

NONIMAGING LIGHT CONCENTRATION USING TOTAL
INTERNAL REFLECTION FILMS

By

Guy René Ouellette

B. Sc. (Physics) University of Manitoba

A THESIS SUBMITTED IN PARTIAL FULFILLMENT OF
THE REQUIREMENTS FOR THE DEGREE OF
MASTER OF SCIENCE

in

THE FACULTY OF GRADUATE STUDIES
PHYSICS

We accept this thesis as conforming
to the required standard

THE UNIVERSITY OF BRITISH COLUMBIA

August 1991

© Guy René Ouellette, 1991

In presenting this thesis in partial fulfilment of the requirements for an advanced degree at the University of British Columbia, I agree that the Library shall make it freely available for reference and study. I further agree that permission for extensive copying of this thesis for scholarly purposes may be granted by the head of my department or by his or her representatives. It is understood that copying or publication of this thesis for financial gain shall not be allowed without my written permission.

Department of Physics

The University of British Columbia
Vancouver, Canada

Date 23 August 1991

Abstract

Here is presented a method of fabricating nonimaging light concentrators from total internal reflection film (TIRF). Prototypes have been made and tested, and found to operate in agreement with predictions of ray-tracing codes. The performance is comparable with that of concentrators made from specular reflecting materials.

Table of Contents

Abstract	ii
List of Tables	v
List of Figures	vi
Acknowledgement	viii
1 Light Concentrators and the Sudbury Neutrino Observatory	1
1.1 Introduction	1
1.2 The Solar Neutrino Problem	1
1.3 The Sudbury Neutrino Observatory	2
1.4 Experimental Program	5
1.5 The Need for Concentrators	6
1.6 Problems Posed by Ultra-Pure Water	7
2 Theory of Nonimaging Concentrators	9
2.1 Lagrange Invariant or Étendue	9
2.2 The Edge-ray Principle	11
2.3 Geometrical Construction of the Concentrator	13
3 Total Internal Reflection Film	21
3.1 Basic Mechanism	21
3.2 Reflecting Modes : Two-Dimensional Analysis	23

3.3	Transmitting Modes	26
3.4	Orientation of TIRF	27
3.5	Construction of a TIRF Concentrator	28
4	Computer Simulations	30
4.1	Computer Algorithms	30
4.1.1	Moorhead's Original Computer Code	30
4.1.2	The UBC Version	33
4.2	Results of the Simulations	37
4.2.1	The Effect of a Polygonal Cross-section	37
4.2.2	The Reflection Properties of Flat TIRF	41
4.2.3	The Effect of the Reflection Properties of TIRF	44
5	Prototype Tests and Results	47
5.1	Data Taken at Oxford	47
5.2	TIRF tests at UBC	49
5.2.1	Experimental Apparatus	50
5.2.2	Data Acquisition	52
5.3	Results	54
5.4	Aluminum tests at UBC	57
6	Discussion	59
	Bibliography	61

List of Tables

4.1	Performance at $\theta = 0^\circ$ incidence.	39
4.2	Performance near the cut-off angle.	41
4.3	Optical properties of Polycarbonate Plastic.	43

List of Figures

1.1	The geometry of the SNO detector.	3
1.2	Wavelength distribution of detected photons.	4
2.3	Étendue.	10
2.4	Illustrating the edge-ray principle for the Winston cone.	12
2.5	The generalized edge-ray principle for a concentrator of arbitrary shape.	13
2.6	Geometry for the concentrator.	14
2.7	Detail of the previous diagram around the point P	15
2.8	Path of an arbitrary ray	16
2.9	Critical angles.	17
3.10	Cross Section of Total Internal Reflection Film.	22
3.11	Basic mechanism.	22
3.12	Illustrating the anti-specular mode of reflection.	24
3.13	Illustrating the specular mode of reflection.	25
3.14	Illustrating a transmitting mode.	26
3.15	The effects of the orientation of TIRF.	27
3.16	Template for a sheet of TIRF used in building the concentrator.	29
4.17	Flow diagram for Moorhead's code.	31
4.18	Cross section of a cell.	35
4.19	Flow diagram for UBC code.	36
4.20	The profile is different in two orientations.	38
4.21	Relationship of the exit aperture to the absorber.	38

4.22	The performance curve for different cross-sections.	40
4.23	Detail of the previous curve.	40
4.24	Two response ratio curves for a dodecagonal concentrator.	42
4.25	Reflection from multiple layers of TIRF in air.	44
4.26	Reflection from multiple layers of TIRF in water.	45
4.27	Performance of an idealized circular-section TIRF concentrator in air. .	46
4.28	Performance of an idealized circular-section TIRF concentrator in water.	46
5.29	The performance of the first UBC prototype.	48
5.30	Experimental apparatus	51
5.31	The data acquisition system.	53
5.32	Map of the efficiency variations on the photocathode.	54
5.33	TIRF in air on the long rotating arm (99 cm).	55
5.34	TIRF in air in the smaller tank (75 cm).	56
5.35	TIRF in water in the smaller tank (75 cm).	56
5.36	Aluminum cone in the smaller tank (75 cm).	58

Acknowledgement

I would like to express gratitude to the Natural Sciences and Engineering Research Council (NSERC) for financial support, enabling me to pursue my studies and my research. I would also like to extend thanks to my supervisor, Dr. C. E. Waltham, for his support and useful criticism, to Dr. R. Schubank for help with the photomultiplier arrangement, to Mr. A. Poon for determining the optical properties of TIRF, and to Mr. I. Yhap for technical support.

Chapter 1

Light Concentrators and the Sudbury Neutrino Observatory

1.1 Introduction

The Sudbury Neutrino Observatory (SNO) will be a large heavy water Čerenkov detector placed deep in a nickel mine in Sudbury, Ontario, Canada. Its purpose is primarily to detect the highest-energy solar neutrinos. These neutrinos come mainly from the β -decay of 8B , which has an endpoint energy of $15MeV$. The project was funded in January 1990, and construction is expected to be complete in 1995. Data is scheduled to be taken over the following five years.

1.2 The Solar Neutrino Problem

The energy generation processes in the core of the sun have been studied theoretically for many years and a model has been developed which predicts that large fluxes of neutrinos are emitted steadily from the solar core. Since about 1970, Davis and his co-workers [4] have been using a Cl detector to measure the flux of the highest energy (8B) neutrinos, and have found it to be about a factor of three lower than that predicted by the Standard Solar Model (SSM) [8]. In April 1989 the Kamiokande collaboration reported results [9] from a large H_2O Čerenkov detector which confirmed the low flux.

This discrepancy could arise because of inadequacies in the SSM or because of previously unobserved properties of neutrinos. The discrepancy has become known as the Solar Neutrino Problem (SNP).

Because both experiments measure only the number of ν_e reaching the earth, it is impossible to tell if there are too few ν_e emitted by the sun or if the ν_e change into another, undetectable, form of neutrino on their way to the earth. Transformation of neutrinos from one type to another can occur if the different types have different masses and there is mixing between them. This effect is called neutrino oscillation, and is predicted by some Grand Unified Theories of particle physics.

In addition to neutrino oscillations *in vacuo*, there is also the possibility of matter enhanced neutrino oscillations, the MSW effect, described by Mikheyev and Smirnov [10], expanding on work by Wolfenstein [11]. Neutrino oscillations taking place in dense matter could result in a significant enhancement in the conversion of ν_e to other types. Because this effect is dependent on neutrino energy, it can produce large distortions of the energy spectrum of neutrinos reaching the earth.

The use of an “astronomical” observatory provides an opportunity to use the sun as a source of neutrinos, far better than any terrestrial source for a sensitive measurement of neutrino oscillations. The great distances involved ($1.5 \times 10^{11}m$) allow a search for oscillations which would be inaccessible to accelerator measurements.

1.3 The Sudbury Neutrino Observatory

The Sudbury Neutrino Observatory will address the SNP by detecting the flux of ν_e as well as the total flux of all types of ν . It constitutes a *direct counting* experiment, that is, the exact arrival time of each ν will be recorded. This makes possible the establishment of a correlation of neutrino events with a time-dependent source.

The SNO detector will consist of 1 kiloton of D_2O in an acrylic vessel, surrounded by 6000 tons of H_2O and an array of photomultiplier tubes (PMTs), see figure 1.1. The D_2O will serve to convert the neutrinos into electrons; also, the combined water

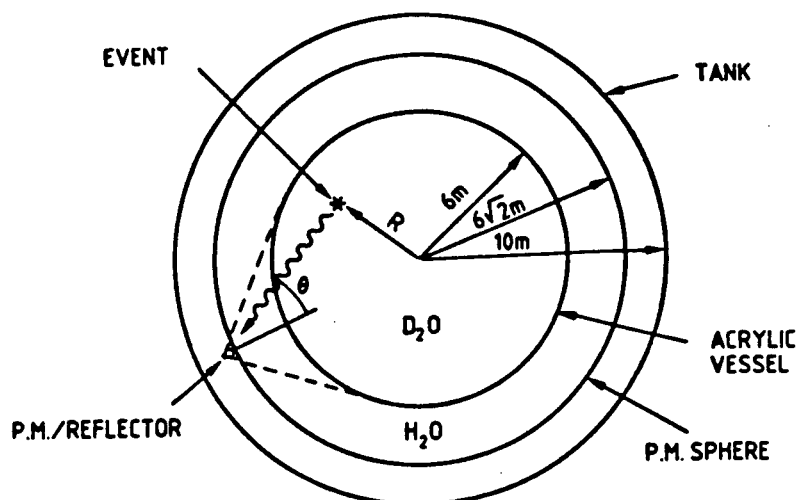


Figure 1.1: The geometry of the SNO detector, with the PMTs and reflectors. The reflectors are designed to provide full coverage of the D_2O , and partial coverage of the H_2O .

volumes will provide electrons to scatter neutrinos. The water will also serve as a moderator for the electrons, producing blue and ultraviolet Čerenkov radiation, which will be detected by the PMTs (see figure 1.2).

Three complementary interactions of neutrinos in D_2O will be observed:

- Charged Current (CC) $\nu_e + d \rightarrow p + p + e^-$ ($Q = -1.44 MeV$)
- Neutral Current (NC) $\nu_x + d \rightarrow \nu_x + p + n$ ($Q = -2.2 MeV$)
- Elastic Scattering (ES) $\nu_e + e^- \rightarrow \nu_e + e^-$

The CC reaction is unique to SNO, and is sensitive only to ν_e . This will permit a determination of high-energy ν_e from the solar core. The large cross section will result in about 7 events per day (assuming 1/3 SSM) with a threshold of 6.5 MeV. This is 30 times more than existing direct counting experiments. The reaction also offers some directional information and would identify the sun as the source of neutrinos.

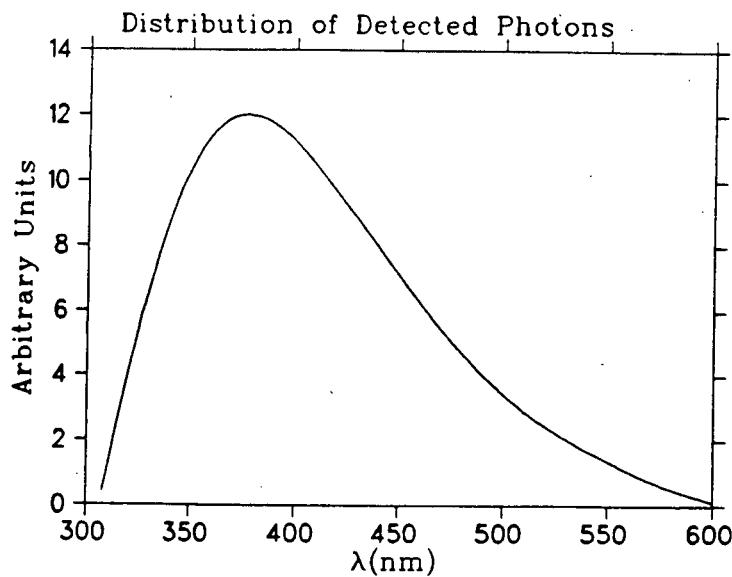


Figure 1.2: Wavelength distribution of detected photons.

The NC reaction is also unique to SNO and will work with any type of neutrino with an energy of more than 2.2MeV. The event rate will be 7 events a day (assuming full SSM) with the expected light detection threshold.

By comparing the rates for the CC and NC reactions, neutrino oscillations could be established. The CC reaction offers electron spectral information, through the relation $E_\nu = E_e + 1.442\text{MeV}$, where E_ν is the neutrino energy, E_e is the electron energy, and the constant arises from the difference between the masses of the deuteron and the protons. This would allow direct observation of the distortions of the energy spectrum produced by the MSW effect.

The ES reaction is dominated by the ν_e , with the cross section for other types a factor of six lower. It offers excellent directional information, but little information about the ν_e energy.

These interactions produce Čerenkov light either directly from the electrons (CC

and ES) or following radiative capture of the neutron (NC), although it may be possible to detect the neutrons directly with ^3He proportional counters inserted later in the D_2O . The Čerenkov light is detected by the photomultiplier tubes (PMTs) surrounding the D_2O . Signals from these interactions are infrequent and easily confused with similar signals from radioactive backgrounds, and this is a paramount consideration in the design of SNO.

1.4 Experimental Program

The observatory will be located 2km underground: this will reduce the cosmic ray flux by a factor of nearly 10^6 to 24 a day in the D_2O . A large mass of D_2O (1000 tons) will be used in order to maximize the number of neutrino interactions. This D_2O will be in a spherical acrylic vessel 6m in radius; the acrylic will be transparent to blue and ultraviolet light. The vessel will be shielded from radioactivity in the rock by 4m of H_2O . The PMTs will be suspended 2.5m from the vessel in order to prevent radioactivity from their glass envelopes from dissociating the deuterons in the D_2O . The design calls for the use of ultra-pure water with particular emphasis on low Th and U concentration.

For the first year the acrylic vessel will be filled with H_2O , during which time the water quality will progressively improve and the temperature will be lowered to the design $8 - 10^\circ\text{C}$. Data on neutrino interactions (ES) and background will be recorded and analyzed. This information will be similar to that collected by Kamiokande, except that the greater rock overburden and better shielding will make for a much improved signal to background ratio. The statistical accuracy on a measurement of the $^8\text{B } \nu_e$ flux will be at the 7% level after six months of data taking.

After this period, most of the H_2O will be removed and the vessel filled with D_2O . This phase of the experiment is the prime reason for building the detector, and it is expected to be in this configuration for a number of years. All three principal interactions will be observed; the CC interaction rate is about 10 times that of ES, and about 25% of the NC interactions (which have about the same rate as the CC) will be detected. We expect to see a statistical accuracy of 3% on the 8B solar neutrino intensity in about six months, much better than with the H_2O .

How to proceed from here will depend on the results obtained in the first two measurements. Adding H_3BO_3 to the D_2O will have the effect of soaking up the neutron background, thereby enabling us to establish the CC signal even better. Alternatively or sequentially we can add NaCl which will enhance the NC signal (and the neutron background) by a factor of three.

1.5 The Need for Concentrators

It is paramount to capture as much of the Čerenkov radiation emanating from the central vessel as possible. This can be accomplished by covering its surface completely with PMTs, but it would be more economical to use a lesser number of PMTs in conjunction with light-gathering concentrators. The design proposes to use 9600 PMTs (19cm diameter), and to surround the face of each tube with a cone of light-reflecting material. At the distance of 2.5m from the vessel, 30% of the surface is covered with light sensitive material, i.e. 30% “hard coverage”. These cones will collect light which would otherwise have missed the PMT and reflect it toward the photosensitive surfaces. These concentrators will almost double the light collecting efficiency of the detector to around 55% effective coverage. By concentrating light, they will make each PMT more sensitive. They will also shield each PMT from light produced in adjacent tubes due to

radioactivity in the glass. The transit time spread (TTS) for photoelectrons over the surface of the photocathode will be about 3ns FWHM. Consequently we can anticipate superior detector performance, particularly in background rejection.

1.6 Problems Posed by Ultra-Pure Water

The concentrators must reflect blue and ultra-violet light efficiently, and survive for 10 years in ultra-pure water. Finding a suitable reflecting material has been difficult.

Aluminum would be a natural choice for reflecting light efficiently in the blue and ultraviolet parts of the spectrum. However, in late 1988 it appeared that conventional aluminum reflecting surfaces would pose severe problems in the SNO detector because of the corrosive environment of ultra-pure water, and because of radioactive backgrounds caused by impurities (Th or U) in the aluminum or supportive glass substrates. Also, aluminum generates high energy gamma rays when it is bombarded by alpha particles. In addition, aluminum would need to be sealed in order to avoid leaching into the ultra-pure water.

In contrast, polymers are known to have low levels of Th and U, on the order of a few parts per trillion. The problem of high-energy gamma rays is nonexistent for the case of polymers. It is known that some polymers leach very little, on the order of $1\mu\text{g}/\text{cm}^2/\text{year}$.

Thus, we were led to investigate the possibility of creating light concentrators out of non-metallic total internal reflection film (TIRF). TIRF is a transparent plastic film, made of acrylic or polycarbonate, which is intended for use in light-pipe systems. One surface is flat, the other is prismatic (see Chapter 3). If the light is transmitted by the first surface, it is likely to undergo total internal reflection at the opposite surface

(hence the name). This material has none of the disadvantages of aluminum or other metals; however, the reflection mechanism is different, and it is not straightforward to assess its reflection properties.

This thesis describes the effort to create a light concentrator out of TIRF, and to assess its light-gathering capacities.

Chapter 2

Theory of Nonimaging Concentrators

The theory of nonimaging concentrators presented here will draw from the work of Welford and Winston [2]. Nonimaging concentrators are optical systems designed to collect as much light as possible through an entry (or input) aperture, and to concentrate this light as much as possible through an exit (or output) aperture, and onto an absorber. For some angles of incidence, a portion of the incident rays are actually reflected back through the entry aperture. Maximum concentration can be accomplished over a range of incident angles, but at the expense of the imaging properties. However, we are not interested in imaging properties, since our concentrator will be coupled to a PMT, which is *not* an imaging device.

Welford and Winston use two concepts to derive the optimal shape of the concentrator : the invariance of the étendue (or conservation of phase space), and the edge-ray principle. We now turn to the explanation of these concepts.

2.1 Lagrange Invariant or Étendue

An important concept in geometrical optics is that of the *Lagrange Invariant*, also known as the *étendue*, *extent*, or *throughput* . Liouville's theorem of the conservation of phase space implies that the étendue is invariant. This means that at any stage of the progress of a light beam through an optical system, the étendue can be evaluated, and found to be the same throughout.

Consider a ray going from a point P in an input medium of refractive index n to

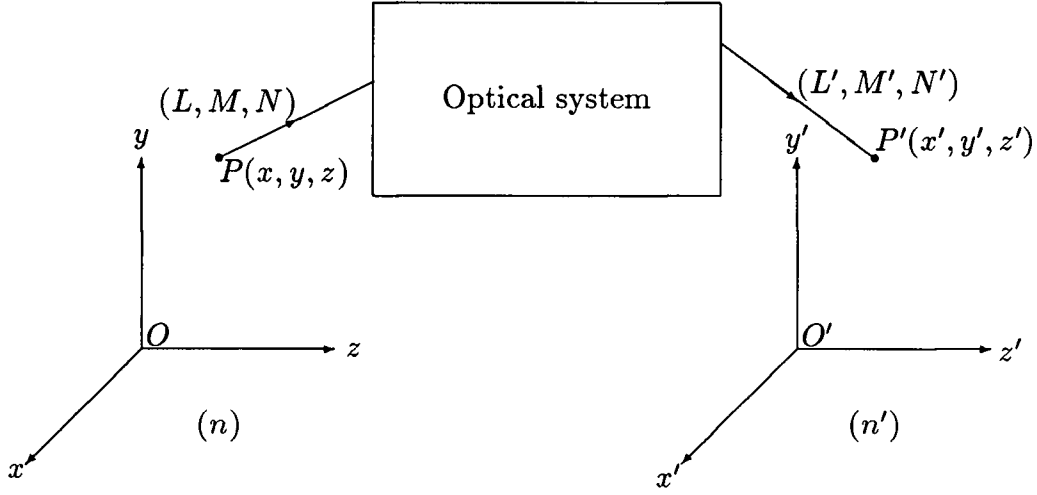


Figure 2.3: Étendue.

a point P' in an output medium of refractive index n' . This ray can be reflected and refracted many times between these two media. Choose coordinate systems $Oxyz$ and $O'x'y'z'$, in the input and output media, respectively, such that the z and z' axes run along the ray, and are never perpendicular to it. Denote the coordinates of the point P by (x, y, z) , and its direction cosines by (L, M, N) (similarly for the point P'). (See figure 2.3). Then a beam of cross section $dx dy$ and angular extent $dL dM$ is generated around the point P by varying the position by dx and dy , and the direction cosines by dL and dM (similarly for the point P').

The Lagrange invariant for a 3-dimensional system, in differential form, is defined thus:

$$n^2 dx dy dL dM = n'^2 dx' dy' dL' dM' \quad (2.1)$$

For the case of a cylindrically symmetric concentrator, the input aperture radius is a , the output aperture radius is a' , the input angular extent (or collection angle) is θ , and the output angular extent θ' . Integrating equation (2.1) with these limits of integration yields the following relation :

$$\iiint n^2 dx dy dL dM = n^2 (\pi a^2) (\pi \sin^2 \theta) = n'^2 (\pi a'^2) (\pi \sin^2 \theta') \quad (2.2)$$

The *geometrical concentration ratio* C for a three-dimensional optical system is defined as the ratio of the input aperture area to the output aperture area. Using this definition and the Lagrange invariant from eq. (2.2) leads to the expression :

$$C = \frac{\pi a^2}{\pi a'^2} = \left(\frac{n' \sin \theta'}{n \sin \theta} \right)^2 \quad (2.3)$$

For a given θ , C is maximum when $\theta' = \pi/2$, and thus the *theoretical maximum concentration ratio* is :

$$C_{max} = \left(\frac{n'}{n \sin \theta} \right)^2 \quad (2.4)$$

These ratios are idealizations, however. In their derivation, it was implicitly assumed that all the incident rays within the collection angle made it to the exit aperture. In actual cases, it is possible that *some* rays within the input angular extent are actually reflected back through the entry aperture. Nonimaging concentrators typically involve a large number of non-paraxial rays, and thus determining the actual *optical concentration ratio* requires an analysis based on ray-tracing methods. In real cases, allowance must also be made for a variety of losses : absorption, error in fabrication, etc.

2.2 The Edge-ray Principle

In the theoretical discussion above, it was assumed that a concentrator could be designed such that all the rays incident within a collection angle θ_i would emerge in a

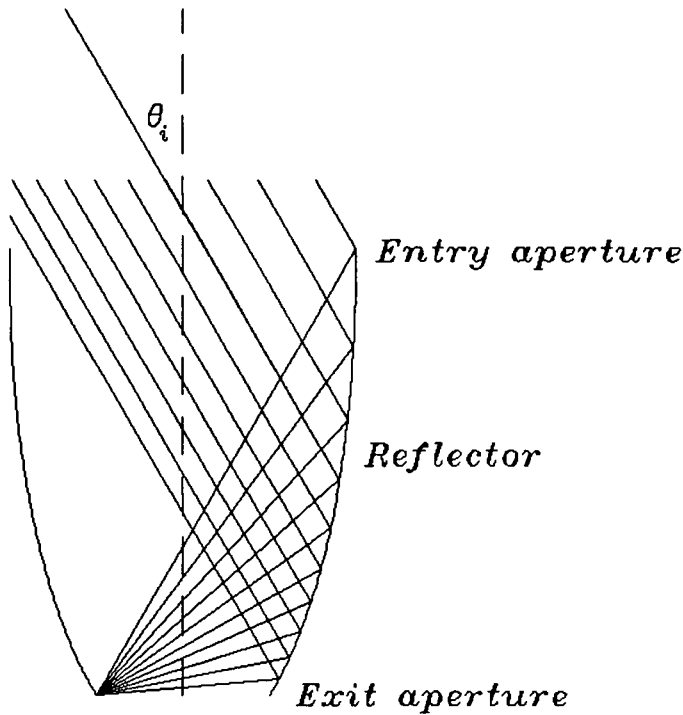


Figure 2.4: Illustrating the edge-ray principle for the Winston cone. The extreme rays are incident at an angle of θ_i with respect to the symmetry axis (dashed). The extreme rays strike the reflector at various positions, but they are all reflected to the same point.

cone of angle $\theta' = \pi/2$. The edge-ray principle of Welford and Winston gives a prescription for achieving this. In its simple form, the edge-ray principle states that the concentrator should be designed such that, after the first reflection, the extreme rays are sent to the rim of the exit aperture. (The extreme rays are the rays incident upon the entry aperture at an angle θ_i). This simple form of the principle is appropriate for a flat absorber and aperture, and it yields the Winston cone (see [2, Appendix D], and figure 2.4).

The edge-ray principle can be generalized for an absorber of arbitrary shape. In this form, the extreme rays are required to be reflected by the concentrator in such a way that they graze the absorber. Thus, if the incident angle is less than θ_i , the ray is

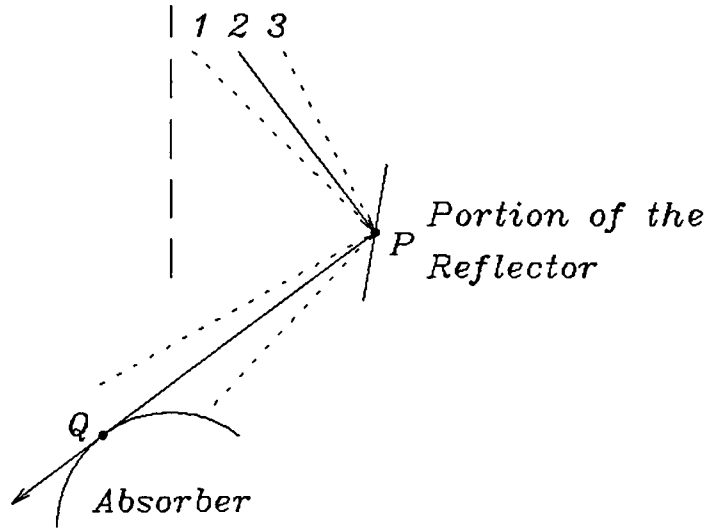


Figure 2.5: The generalized edge-ray principle for a concentrator of arbitrary shape.

reflected into the absorber; if the incident angle is greater than θ_i , the ray misses the absorber. In figure 2.5, the ray labelled 2 is a typical extreme ray, incident at angle θ_i with respect to the symmetry axis. It strikes the reflector at the point P , and the reflected ray is tangent to the absorber at the point Q . Ray 1 is incident at an angle greater than θ_i , and it is obvious from the figure that it will miss the absorber. Ray 3 is incident at angle less than θ_i , and it is reflected into the absorber. In the ideal concentrator, the collection angle is also a cut-off angle : all the rays beyond this cut-off angle are reflected back through the entry aperture.

2.3 Geometrical Construction of the Concentrator

The three-dimensional concentrator will be generated by rotating the two-dimensional profile around the optic axis. Consider an extreme ray with direction vector \hat{k} (see

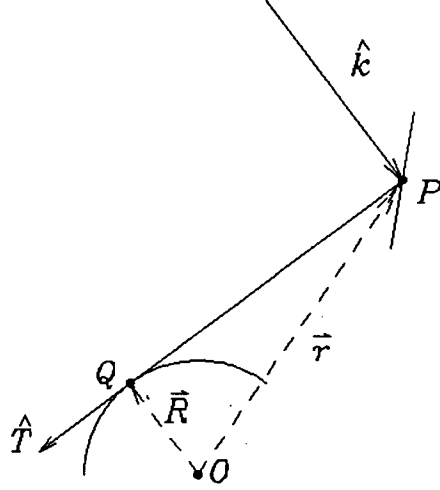


Figure 2.6: Geometry for the concentrator. The extreme ray is incident along the vector \hat{k} , and it strikes the concentrator at the point P . The reflected ray grazes the absorber at the point Q , where the tangent is \hat{T} .

figure 2.6). It strikes the profile of the concentrator at the point P , where the tangent to the profile is \hat{t} , and the normal to the profile is \hat{n} . The ray is reflected, and it grazes the absorber at the point Q , where the tangent is \hat{T} . By the edge-ray principle the reflected ray has direction vector \hat{T} . Choose the point O as origin, and let the vector \vec{r} denote the position vector from O to P , and let the vector \vec{R} denote the position vector from O to Q . If w denotes the distance between P and Q , then the position vectors are related by:

$$\vec{R} = \vec{r} + w\hat{T} \quad (2.5)$$

The law of reflection states that the vector difference $\hat{k} - \hat{T}$ is perpendicular to the tangent \hat{t} , where \hat{k} is the incident ray, and \hat{T} is the reflected ray (see figure 2.7). The

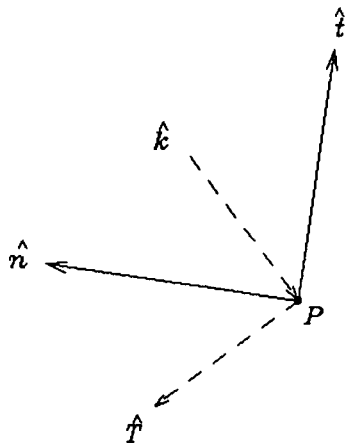


Figure 2.7: Detail of the previous diagram around the point P . The ray is incident along the unit vector \hat{k} , and the reflected ray is along the vector \hat{T} . The unit tangent vector of the profile of the reflector is \hat{t} , and the unit normal is \hat{n} .

profile of the concentrator is thus governed by :

$$(\hat{k} - \hat{T}) \cdot \hat{t} = 0 \quad (2.6)$$

The profile is not completely specified by Eq. (2.6) : some boundary conditions would need to be applied. Typically, a further complication arises : part of the absorber is inaccessible to the extreme rays. The solution adopted by Welford and Winston is to continue the profile of the reflector up to the absorber using an involute curve, which obeys the equation:

$$\hat{T} \cdot \hat{t} = 0 \quad (2.7)$$

In the case at hand, the absorber, the PMT, is approximately spherical. If its radius is R , and its polar extent is θ_c , then the exit aperture radius is $a' = R \sin \theta_c$. We choose a coordinate system where the z -axis is along the symmetry axis of the reflector, and the y -axis is perpendicular to it. The origin is chosen as the centre of the sphere. The

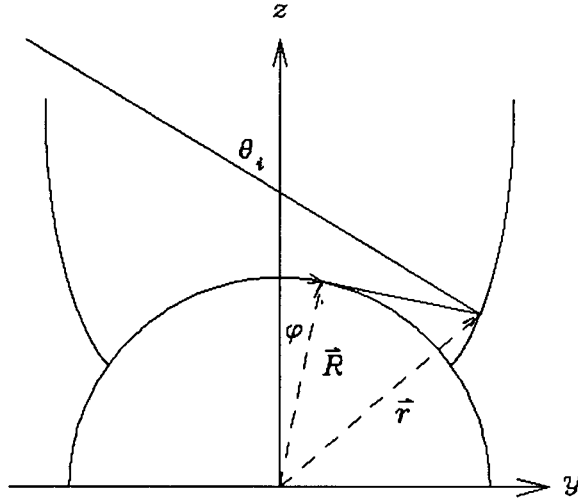


Figure 2.8: Path of an arbitrary ray. The ray enters at an angle θ_i , reflects on the concentrator at the point $\vec{r} = (y(\varphi), z(\varphi))$, and grazes the absorber at the point $\vec{R} = (Y(\varphi), Z(\varphi))$.

coordinates on the reflector are denoted by:

$$\vec{r} = (y, z) \quad (2.8)$$

while the corresponding coordinates on the absorber are given by:

$$\vec{R} = (Y, Z) = (R \sin \varphi, R \cos \varphi) \quad (2.9)$$

The angular coordinate φ is the polar angle: it is the angle between the z -axis and the radius vector from the origin to the point on the absorber. (See figure 2.8). In this coordinate system, the extreme rays run along the direction vector

$$\hat{k} = (\sin \theta_i, -\cos \theta_i) = \sin \theta_i \hat{y} - \cos \theta_i \hat{z}, \quad (2.10)$$

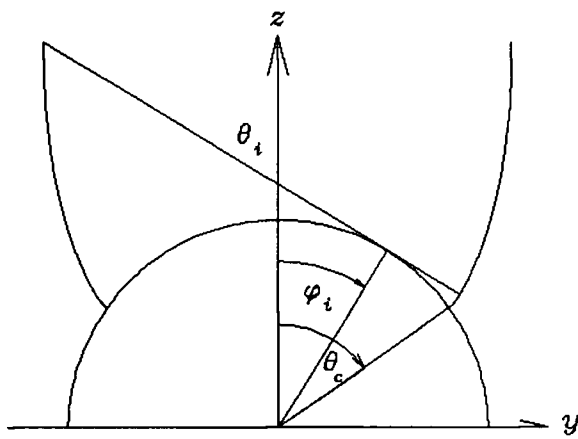


Figure 2.9: Critical angles. The last extreme ray enters at an angle θ_i , and grazes the absorber at the angular coordinate $\varphi_i = \pi/2 - \theta_i$. The absorber has an acceptance angle θ_c . The region from φ_i to θ_c is inaccessible to the extreme rays: it is a shadow section.

The unit tangent to the absorber is defined with a minus sign in order to agree with the direction and sense of the reflected ray :

$$\hat{T} = -\frac{d\vec{R}}{d\varphi} / \left| \frac{d\vec{R}}{d\varphi} \right| \quad (2.11)$$

$$\hat{T}_y = -\cos \varphi \quad (2.12)$$

$$\hat{T}_z = \sin \varphi \quad (2.13)$$

Equation (2.5) becomes:

$$\begin{aligned} \vec{r} &= (y, z) = \vec{R} - w(\varphi)\hat{T} \\ y(\varphi) &= Y - w(\varphi)\hat{T}_y(\varphi) \\ &= R \sin \varphi + w(\varphi) \cos \varphi \end{aligned} \quad (2.14)$$

$$\begin{aligned} z(\varphi) &= Z - w(\varphi)\hat{T}_z(\varphi) \\ &= R \cos \varphi - w(\varphi) \sin \varphi \end{aligned} \quad (2.15)$$

The involute is governed by equation (2.7) ; equations (2.14) and (2.15) are differentiated to yield \hat{t} (normalization is not necessary). The involute intersects the sphere at the point with angular coordinate θ_c . The shadow section is determined by the point where the extreme ray directly strikes the PMT tangentially ; its angular coordinate is $\varphi_i = \pi/2 - \theta_i$. The involute intersects the sphere at the point $\varphi = \theta_c$, hence we require $w(\theta_c) = 0$. After some straightforward manipulations, $w(\varphi)$ is found to be

$$w(\varphi) = R(\theta_c - \varphi), \quad \text{where } \varphi_i \leq \varphi \leq \theta_c \quad (2.16)$$

The same approach transforms equation (2.6) into

$$0 = R[1 + \cos(\varphi - \varphi_i)] + [1 + \cos(\varphi - \varphi_i)] \frac{dw}{d\varphi} - w \sin(\varphi - \varphi_i) \quad (2.17)$$

$$\text{or} \quad 0 = R[1 + \cos(\varphi - \varphi_i)] + \frac{d}{d\varphi}[w(\varphi)(1 + \cos(\varphi - \varphi_i))] \quad (2.18)$$

This is a simple first-order differential equation, whose solution is

$$w(\varphi) = R \frac{(\Delta - \varphi - \sin(\varphi - \varphi_i))}{1 + \cos(\varphi - \varphi_i)} \quad (2.19)$$

The constant Δ is determined by fitting this curve smoothly to the involute part. The range of φ is determined by the point where $dy/d\varphi = 0$; this is where $\varphi = -\varphi_i$. Thus the main portion of the curve is described by

$$w(\varphi) = R \frac{(2\theta_c - \varphi_i - \varphi - \sin(\varphi - \varphi_i))}{1 + \cos(\varphi - \varphi_i)}, \quad \text{where } -\varphi_i \leq \varphi \leq \varphi_i \quad (2.20)$$

It is convenient to express the concentration ratio in terms of the quantities defined above. The exit aperture has radius a' and is determined by the point where the concentrator touches the absorber, thus:

$$a' = y(\theta_c) = R \sin \theta_c \quad (2.21)$$

The entry aperture radius a is defined by $y(-\varphi_i)$, where

$$y(-\varphi_i) = R \sin(-\varphi_i) + R w(-\varphi_i) \cos(-\varphi_i), \quad (2.22)$$

$$w(-\varphi_i) = \frac{2\theta_c + \sin(2\varphi_i)}{1 + \cos(2\varphi_i)} = \frac{\theta_c + \sin \varphi_i \cos \varphi_i}{\cos^2 \varphi_i} \quad (2.23)$$

After some straightforward algebra, we get this simple expression for the entry aperture radius:

$$a = y(-\varphi_i) = \frac{R\theta_c}{\cos \varphi_i} = a' \frac{\theta_c}{\sin \theta_c} \frac{1}{\cos \varphi_i} \quad (2.24)$$

The last equation yields the geometric concentration ratio:

$$C_{max} = \frac{\pi a^2}{\pi a'^2} = \left(\frac{1}{\cos \varphi_i} \right)^2 \left(\frac{\theta_c}{\sin \theta_c} \right)^2 = \left(\frac{1}{\sin \theta_i} \right)^2 \left(\frac{\theta_c}{\sin \theta_c} \right)^2 \quad (2.25)$$

This is to be compared to the result for a Winston CPC cone, which is designed for a flat photocathode (see Welford and Winston, [2]):

$$C_{Flat} = \left(\frac{1}{\sin \theta_i} \right)^2 \quad (2.26)$$

The result is similar, except for a gain factor

$$G = \left(\frac{\theta_c}{\sin \theta_c} \right)^2, \quad (2.27)$$

which goes to 1 as θ_c goes to zero, as it should. It reaches a value of $\pi^2/4 \doteq 2.467$ when $\theta_c = \pi/2$. This gain factor is close to the ratio of the surface area of the photocathode to the flat area of the exit aperture, which is :

$$G' = \frac{2\pi R^2(1 - \cos \theta_c)}{\pi R^2 \sin^2 \theta_c} = \left(\frac{1}{\cos(\theta_c/2)} \right)^2 \quad (2.28)$$

This gain factor also goes to 1 as θ_c goes to zero. However, it reaches a value of only $G' = 2$ for $\theta_c = \pi/2$. This naïve comparison breaks down because there are subtle geometrical effects; for example, the entry aperture radius is different (see equation 2.24: the Winston CPC cone corresponds to the case where $\theta_c \rightarrow 0$ while a' is held constant). If one simply stuck a spherical photocathode at the end of a Winston CPC cone, the actual concentration would be less than ideal, because the CPC cone is not designed for a spherical photocathode.

All the comments above are valid when $\varphi_i < \theta_c$. If $\varphi_i > \theta_c$, then there is no involute portion, and the profile curve needs to be fitted differently. The constant Δ in equation 2.19 is then determined by letting $w(\theta_c) = 0$: this way, the profile curve intersects the sphere at θ_c . Thus in the case where $\varphi_i > \theta_c$, we get the following results:

$$\Delta = \theta_c + \sin(\theta_c - \varphi_i) \quad (2.29)$$

and

$$C_{max} = \frac{\pi a^2}{\pi a'^2} = \frac{1}{\cos^2 \varphi_i} \left(\frac{\theta_c + \varphi_i + \sin(\theta_c - \varphi_i)}{2 \sin \theta_c} \right)^2, \quad \varphi_i = \pi/2 - \theta_i \quad (2.30)$$

Welford and Winston [2] derived a differential equation analogous to Equation 2.18, but for an arbitrary absorber profile. They solved it for the special case of an absorber with a circular cross-section, and $\theta_c = \pi$.

Chapter 3

Total Internal Reflection Film

Total Internal Reflection Film, or TIRF, was developed by Lorne Whitehead [6]. It is a transparent film, made of plastic such as acrylic or polycarbonate. One surface is flat, the other is prismatic (see figure 3.10) . The light is incident upon the flat surface; it is then likely to undergo total internal reflection at the opposite surface (hence the name). The light undergoes multiple reflections and refractions along its path through the faces of TIRF. Eventually, the light ray will either be reflected to the original side of the sheet of TIRF, or else it will emerge on the opposite side (neglecting losses). Whitehead intended to use TIRF as an efficient light guide: light would be guided down a tube of TIRF by multiple reflections, but then it would leak out by controlled transmission in order to provide uniform lighting along its length. Here, we intend to use TIRF solely for its reflective properties.

In figure 3.10, the light enters from the bottom. The TIRF alternates in thickness between the values of t_0 and $t_0 + t_1$, t_1 being the height of the prisms. The width $l = \sqrt{2}t_1$, and the prismatic faces form an angle of $\pi/4$ with the flat surface; also, the thickness t_0 is set equal to t_1 .

3.1 Basic Mechanism

Consider a ray going from the flat surface to one face of the prismatic surface (see figure 3.11). The light ray enters the TIRF at angle θ , and is refracted at an angle α with respect to the normal of the flat surface. It then strikes the tilted face at an angle β

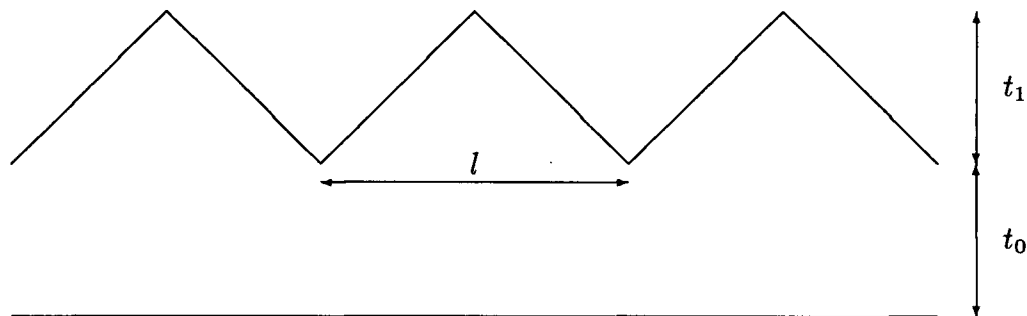


Figure 3.10: Cross Section of Total Internal Reflection Film.

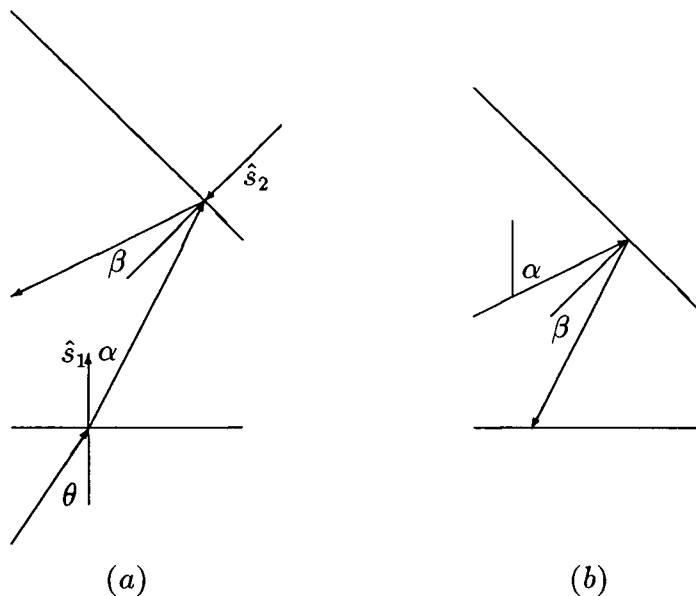


Figure 3.11: Basic mechanism. The angle α is defined clockwise from the normal \hat{s}_1 to the transmitted ray, while the angle β is defined clockwise from the normal \hat{s}_2 to the reflected ray. In (a), $\alpha < \pi/4$, and β is positive. In (b), $\alpha > \pi/4$, and β is negative.

to the normal of that face. If β is within a certain range, then the ray undergoes total internal reflection. Since the prismatic face is tilted at $\pi/4$ radians, the angles α and β are related :

$$\beta = \pi/4 - \alpha \quad (3.31)$$

There are three cases to consider :

1. If $\alpha > \pi/4$, then β is negative, and the ray is sent back to the flat face (downwards, in figure *b*).
2. If $\alpha < -\pi/4$, then the ray will certainly miss the face shown, and strike the opposite face, which is tilted the other way (not shown). But this case is just a mirror image of case 1.
3. If $-\pi/4 < \alpha < \pi/4$, then the ray may strike one or both faces, before re-emerging through the flat face . This depends on the geometry of the TIRF, and on the entry position of the ray.

3.2 Reflecting Modes : Two-Dimensional Analysis

Depending on the incident position angle, the ray may be reflected according to different modes. If $|\alpha| > \pi/4$, then the ray will be reflected once before re-emerging. If $|\alpha| < \pi/4$, then the ray may be reflected two or more times before re-emerging.

One mode of reflection is depicted in figure 3.12. The ray enters the flat surface at the point *a* at an angle θ , and is refracted at an angle α . It is then reflected at the point *b* at an angle $\beta = \pi/4 - \alpha$. Then it is reflected at the point *c* at angle $\pi/2 - \beta = \pi/4 + \alpha$. It re-emerges at the point *d* at an angle α . This mode is called “antispecular”, because the projection of the reflected ray is anti-parallel to the incident ray.

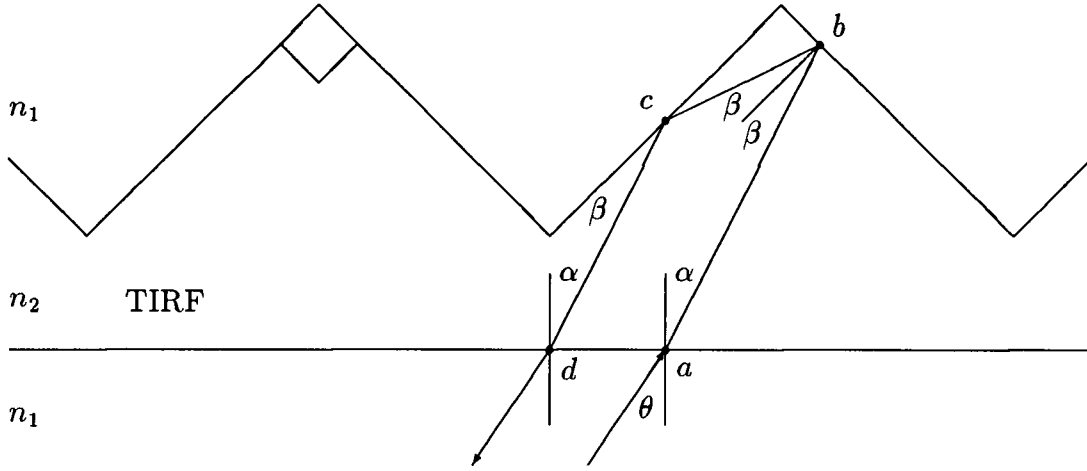


Figure 3.12: Illustrating the anti-specular mode of reflection.

We require that the ray be refracted at points a and d , for all incident angles θ from $-\pi/2$ to $\pi/2$. Thus:

$$|\sin \alpha| < n_1/n_2 \quad (3.32)$$

The angle α has already been restricted to $|\alpha| < \pi/4$, and the condition is satisfied if $n_2/n_1 < \sqrt{2}$. We also require that the ray should undergo total internal reflection at the point b :

$$|\sin \beta| = |\sin(\pi/4 - \alpha)| > n_1/n_2 \quad (3.33)$$

and also at the point c :

$$|\sin(\pi/2 - \beta)| = |\cos \beta| = |\sin(\pi/4 + \alpha)| > n_1/n_2 \quad (3.34)$$

Combining relations 3.32, 3.33, 3.34, leads to the conditions:

$$|\sin \alpha| < |\sin(\pi/4 - \alpha)| \quad (3.35)$$

and

$$|\sin \alpha| < |\sin(\pi/4 + \alpha)| \quad (3.36)$$

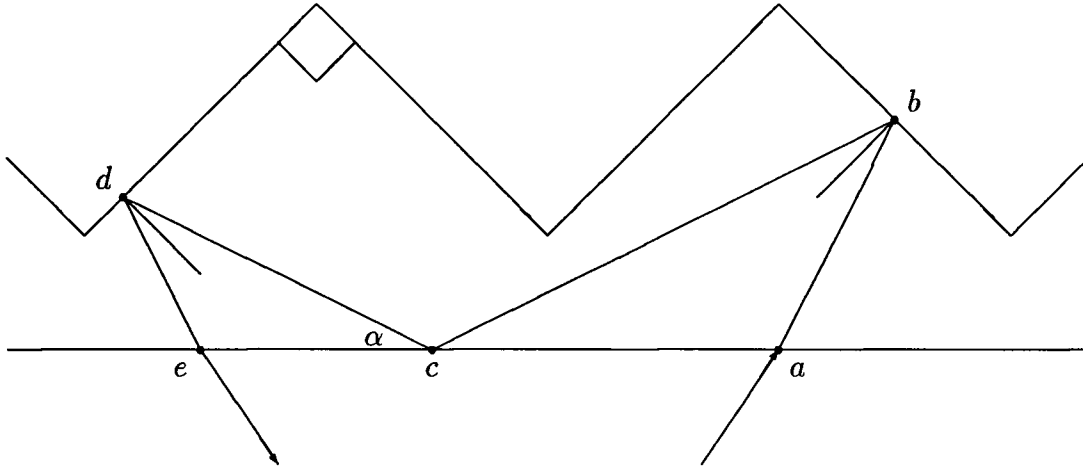


Figure 3.13: Illustrating the specular mode of reflection.

These conditions can be satisfied simultaneously only in the range $-\pi/8 < \alpha < \pi/8$. The ratio n_1/n_2 should be equal to $\sin(\pi/8)$, thus $n_1/n_2 \doteq 1/2.61$. If it is higher, then the relations 3.33 and 3.34 restrict the range of α . If it is lower, then relation 3.32 restricts the range of α .

Another mode of reflection is depicted in figure 3.13. This mode is called “specular”, because the incident and reflected rays behave like ordinary specular reflection. In this case, transmission occurs at the points a and e , which leads to relation 3.32. Reflection occurs at the points b and d , which leads to relations 3.33 twice. There is an additional reflection at the point c , which leads to a new relation :

$$|\sin(\pi/2 - \alpha)| = |\cos \alpha| > n_1/n_2 \quad (3.37)$$

but this relation is already satisfied if 3.32, 3.33, and 3.34 are satisfied.

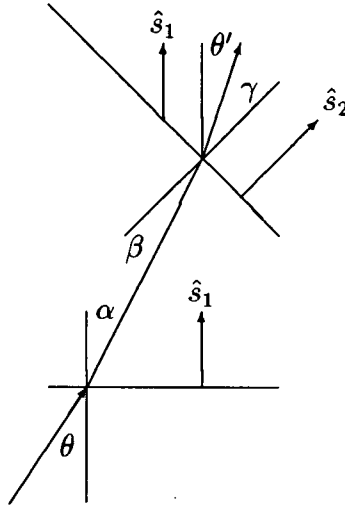


Figure 3.14: Illustrating a transmitting mode.

3.3 Transmitting Modes

In the previous section, it was implicitly assumed that there would always be transmission at the flat face, and reflection at the prismatic faces. This occurs provided $n_2/n_1 \doteq 2.61$. However, in practice, the index of refraction is less than this. Thus it is possible for the ray to be transmitted through the TIRF. It is still useful, though, because there might still be partial reflections. Also, TIRF has a rectifying property. This means that upon emerging from the TIRF, the ray is deflected towards the normal \hat{s}_1 . This way, it has a better chance of being reflected from a second layer.

Consider figure 3.14. The ray, incident at an angle θ , is refracted at an angle α . It comes to the prismatic face at an angle β , and is refracted at angle γ with respect to \hat{s}_2 , or θ' with respect to \hat{s}_1 .

$$\theta' = \frac{\pi}{4} - \gamma = \frac{\pi}{4} - \arcsin(n \sin \beta), \quad |n \sin \beta| < 1 \quad (3.38)$$

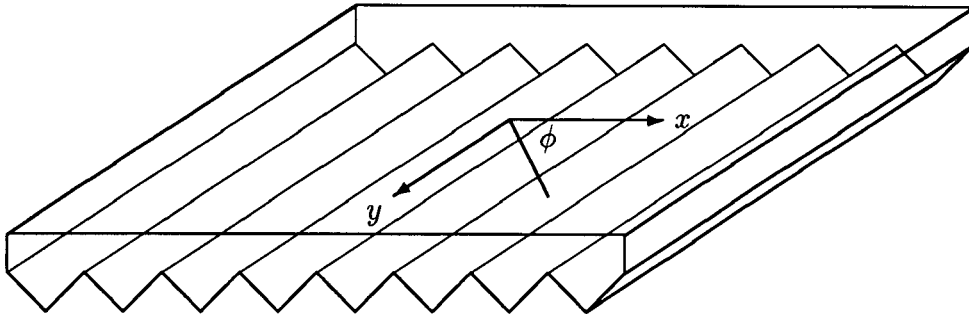


Figure 3.15: The effects of the orientation of TIRF. The y-axis is oriented along the prism axis, or translational axis. The angle ϕ is the angle between the ray and the x-axis. (This convention is different from Whitehead's convention.)

where

$$\beta = \frac{\pi}{4} - \alpha = \frac{\pi}{4} - \arcsin\left(\frac{\sin \theta}{n}\right), \quad -\pi/2 < \beta < \pi/2 \quad (3.39)$$

Total internal reflection occurs when $|n \sin \beta| > 1$. There is rectification when $\cos \theta' > \cos \theta$; the range for which rectification occurs increases with increasing refractive index n . If the ray continues to another layer, it has better chances of being reflected. Thus by using many layers, it is possible to achieve a reasonably reflective 'mirror'.

3.4 Orientation of TIRF

The previous results are valid for two-dimensional TIRF. In order to take the third dimension into account, it is worthwhile to follow Whitehead [6, p.18] and make use of projection-corrected refractive indices, defined as follows :

$$n'_1 = \sqrt{n_1^2 - n_1^2 \sin^2 \phi} \quad (3.40)$$

$$n'_2 = \sqrt{n_2^2 - n_1^2 \sin^2 \phi} \quad (3.41)$$

The two-dimensional case corresponds to $\phi = 0$ (see figure 3.15). The ratio of effective refractive indices, n'_2/n'_1 , increases with ϕ . Thus rays which are more or less aligned with the grooves are reflected more strongly than other rays. If TIRF is to be used to construct a reflector as in chapter 2, then the grooves of the TIRF should be aligned with the z-axis.

3.5 Construction of a TIRF Concentrator

We now consider two possible ways to bend TIR film: *along* the prism axis, or *across* it. When it is bent *along* the axis, each prism gets curved, but the prisms keep their orientation relative to each other. A cross-section perpendicular to the axis shows no change. When it is bent *across* the axis, the prisms remain straight, but they are tilted with respect to each other. This is not recommended, since the TIR film is likely to crack. Fortunately, the orientation of the TIRF dictated by optical considerations allows the construction of a concentrator which follows the profile generated in chapter 2. That is, the TIR film is bent *along* the prism axis, and the prisms run parallel to the optic axis. However, it is impossible to achieve such a concentrator with a circular cross-section, since that would entail bending the TIR film *across* the prism axis. The concentrator must be built with a polygonal cross-section.

We have built such a concentrator. It consists of five layers of TIRF bolted to an acrylic support frame, which surround a central circular opening for a PMT. Each sheet of TIRF has twelve tapered facets, giving the concentrator a dodecagonal cross-section. The facets follow the shape given in chapter 2, in such a way that they meet at the vertices of the dodecagonal cross-section all the way down the symmetry axis of the concentrator. The facets were cut out of the sheet, but leaving a 3cm common band, so that the sheet would stay in one piece. The twelve square tabs at the bottom of the

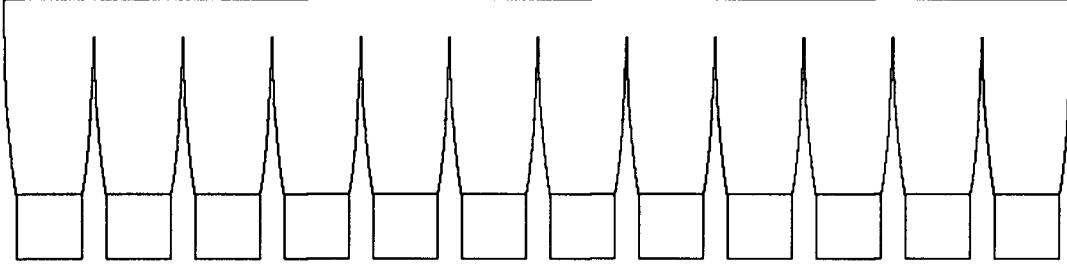


Figure 3.16: Template for a sheet of TIRF used in building the concentrator.

sheet are folded in order to bolt the sheet to the acrylic support, without interfering with the concentrator profile.(see figure 3.16). The next four layers were scaled up for fitting around the first layer.

The concentrator was designed with an exit aperture of $a' = 9.5cm$, polar extent $\theta_c = 54.5^\circ$, and acceptance angle $\theta_i = 58.6^\circ$ (thus $\beta = 31.4^\circ$). These parameters are optimum for SNO. The concentration ratio turns out to be 1.875. The construction method allowed a profile accuracy of $3mm$ to be achieved.

Chapter 4

Computer Simulations

Dr. Martin Moorhead of Oxford Nuclear Physics Laboratories has kindly provided a computer code in order to conduct ray-tracing simulations. This computer code was designed for concentrators with a circular cross-section, made from specular reflecting material. In order to model TIRF concentrators, this computer code needs to be updated on two fronts: first, to deal with the peculiar reflection properties of TIR film, and second, to deal with the polygonal cross-section of the concentrator.

4.1 Computer Algorithms

4.1.1 Moorhead's Original Computer Code

The main program is menu-driven. The first tasks are to define the geometries of the absorber and concentrator: this is carried out by the subroutines PMTSPEC and REFSPEC, respectively. PMTSPEC is quite straightforward: it inputs the parameters specifying the PMT and then passes them on to PMTSPEC. This subroutine, in turn, generates the profile of the concentrator according to the principles of Welford and Winston explained in chapter 2. The profile is digitized, and stored in the arrays R and Z ; the user can control the number of points generated via the variable DL. REFSPEC updates the angular parameter (φ in chapter 2) in such a way that the path length between consecutive points ($R(I), Z(I)$) is equal to DL.

Now the program reaches the menu: the user can initiate ray-tracing by calling the

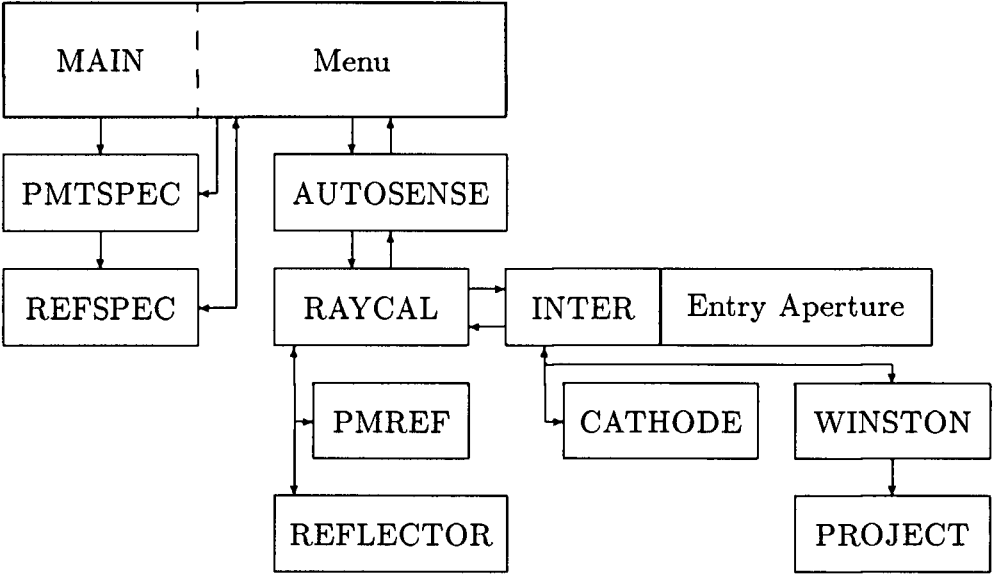


Figure 4.17: Flow diagram for Moorhead's code.

subroutine AUTOSENSE. (There is also a subroutine MANSENSE for two-dimensional concentrators). Alternatively, he can update the PMT or concentrator shapes by calling REFSPEC or PMTSPEC. If he chooses to re-activate PMTSPEC, the program also re-activates REFSPEC, since the shape of the concentrator must be compatible with the absorber.

The ray-tracing is controlled by the subroutine AUTOSENSE. For a given range of input angles θ , it generates the entry position and direction of a great number of rays. The entry position is taken from a square grid encompassing the entry aperture, and AUTOSENSE keeps only the rays which strike within the entry aperture. The performance of the cone is taken as the fraction of these rays which ultimately reach the absorber.

The algorithm assumes that the light is coming from a source at infinity, hence, the direction vector is determined by the angle θ . The algorithm generates the same number of points on the entrance aperture regardless of the incident angle θ ; the density of rays is constant in a plane parallel to the entrance aperture. It is more appropriate to use a normalization such that the density of rays is constant in a plane perpendicular to the input beam. This can be corrected simply by multiplying each point on the simulated performance curve by $\cos \theta$.

Next, AUTOSENSE calls RAYCAL to determine the outcome of each ray, and collates these results for each input angle. RAYCAL, in its turn, calls the subroutine INTER repeatedly until a definite outcome is reached. As it progresses through the optical system, the ray can be reflected by the concentrator, it can be reflected back out through the entry aperture, or it can strike the absorber. Ideally, a final outcome occurs when the ray is either reflected back out, or when it is absorbed with perfect efficiency by the photocathode. However, the reflectance of the concentrator is not ideal, and the tube is not perfectly sensitive. There are thus losses at every step in the

progress of the ray. INTER keeps track of these and returns the results to RAYCAL.

First, INTER tests whether the ray is coming back out through the entry aperture. If it is not escaping through the entry aperture, then INTER calls the subroutine CATHODE to determine whether the ray strikes the spherical photocathode, and if so, where. If it does not strike the PMT, then INTER assumes that the ray must be heading for the concentrator, and calls the subroutine WINSTON to determine the intersection. This cycle is repeated until a final outcome is reached.

As the ray progresses, RAYCAL updates variables on a pro rata basis to keep track of how much of the ray is absorbed or sensed by the various elements of the system. It uses the subroutine REFLECTOR to determine how much of the ray is reflected and absorbed by the concentrator, and to update the direction vector. It uses the subroutine PMREF to determine how much of the ray is absorbed, reflected, or sensed by the PMT, and to update the direction vector if the ray is reflected.

The subroutine WINSTON is used to determine the intersection of the ray with the concentrator. The profile is in a digitized form, and the shape is approximated by a series of truncated cones. The subroutine first projects the ray onto the small cone at the bottom of the concentrator (or at the top), that is, the cone which is generated by the points $(R(0), Z(0))$ and $(R(1), Z(1))$. Then it digitizes the z-coordinate of this point, and uses this new cone likewise. The subroutine iterates these approximations until the intersection is between the digitized generators of the cone.

4.1.2 The UBC Version

A number of changes had to be made in order to accommodate the polygonal TIRF cone. First, a new subroutine, TIRFSPEC, was introduced into the menu in order to let the user specify the characteristics of TIR film and the number of layers. Second, the subroutine REFLECTOR had to incorporate a new subroutine called TIRF in order

to deal with the peculiar optical properties of TIR film.

The subroutine TIRF traces the light ray through the layers of TIR film. The problem is subdivided into cells, each cell containing a single prism (see figure 4.18). Each cell consists of two parts: a plastic prism, and a gap of water or air. The subroutine TIRF follows the progress of the ray through the cell using cell coordinates; when the ray reaches a new cell, the cell coordinates are updated, and the algorithm keeps track of the number of rows and layers crossed by the ray.

At each refractive interface (boundaries 1, 3 or 4), the subroutine TIRF uses the subroutine REFRACT in order to calculate the reflected and transmitted angles, and to choose refraction or reflection, depending on the reflectance. The angles and the reflectance depend on the refractive indices of the plastic and water. The refractive indices depend in turn on the wavelength of the incident light: the refractive index of plastic ranges from 1.676 to 1.580 over the wavelength range $300 - 600nm$, and the refractive index of water ranges from 1.347 to 1.333. The subroutine INDEX generates the refractive indices randomly, in accordance with the wavelength distribution described by figure 1.2 of Chapter 1.

There were also geometrical considerations. The profile could no longer be split into nice, analytical cones. The concentrator no longer fit the PMT, and the algorithm had to account for the gaps. Other changes were required by the experimental set-up. POINTSENSE does the same job as AUTONSENSE, but for a source a finite distance away. The algorithm chooses a random point on a conical section of the unit sphere centered on the point source. This generates a direction vector, and by extending the ray to the entry plane, a candidate position is generated. The algorithm keeps only the rays whose entry positions are within the entry aperture. With these conventions, the algorithm simulates a point source of uniform intensity. If this source were infinitely

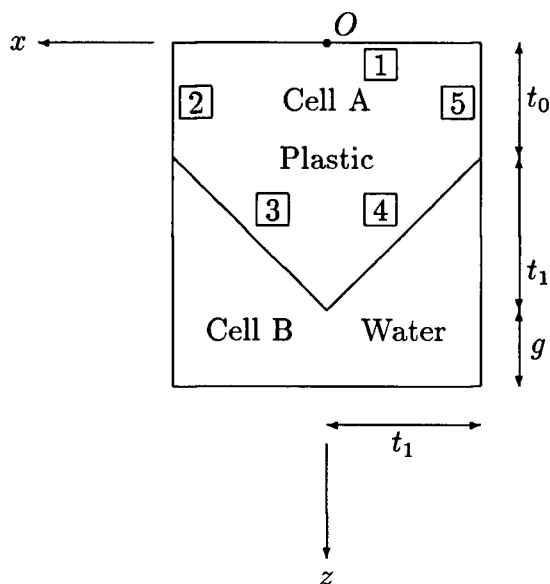


Figure 4.18: Cross section of a cell.

far away, it would produce a constant density of rays in a plane perpendicular to the input beam.

The subroutine PMPREF was supplemented with a new subroutine, PMTEFF, to compensate for measured efficiency inhomogeneities on the PMT.

Finally, I introduced some changes which were not necessary, but were useful. The subroutines RAYCAL and INTER were merged into a single one, since they always required simultaneous debugging. The progress of the ray was followed according to the Monte Carlo method: instead of updating all variables simultaneously on a pro rata basis, the algorithm would choose a particular outcome randomly in accordance with the reflectance or absorption (interpreted as an outcome probability).

The first attempt at an updated version of WINSTON used Moorhead's approach to find the intersection of the ray with each facet, and choose the right one. Obviously, this was not very efficient. The next step was to use a virtual round concentrator to guess which petal would be hit. This failed occasionally, when the ray was almost

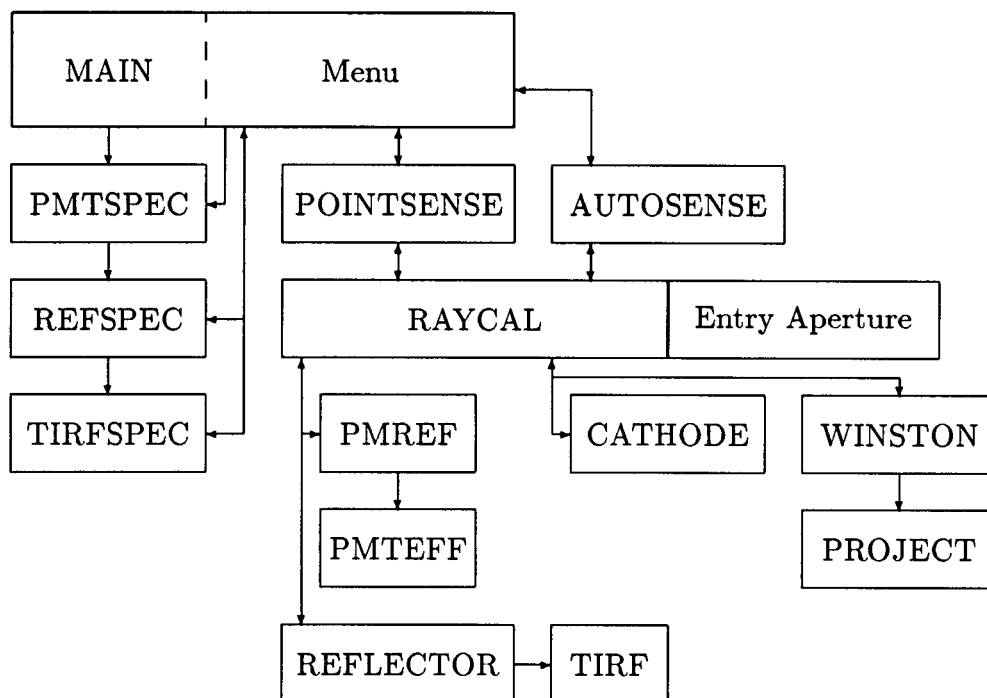


Figure 4.19: Flow diagram for UBC code.

tangential to the concentrator (in the projected x - y plane), and it skipped to the next facet. This problem was fixed by using a round concentrator which *circumscribed* the polygonal cone. However, in this case, the algorithm failed when the ray came too close to the top or the bottom of the concentrator.

Eventually, I opted for a completely different approach. Now, WINSTON divides the concentrator in slices sandwiched by planes $z = Z(I)$. It starts with two planes at the extremes of the possible range of z -values for the intersection, and projects the ray onto them. Then it halves this range, at each step testing whether the projections lie inside or outside the polygonal cross-section (using the subroutine POLYGIN). It keeps the pair of planes which have opposite scores, and thus zeroes in on the slice containing the intersection. It is then relatively easy to determine the actual intersection.

4.2 Results of the Simulations

For the purposes of the simulations, we chose a concentrator according to the parameters of Chapter 3, with an exit aperture radius of 9.5cm , a polar extent of 54.5° , and a cut-off angle of 58.6° . For simplicity, we chose the subroutine AUTONSENSE, which generates light in parallel rays. This permits separating the effect of distance from the other effects. The performance curve gives the percentage of the rays incident upon the entrance aperture which are sense by the PMT, as a function of incident angle. The response ratio is defined as the ratio of the number of rays received by the PMT, with and without the concentrator. The response ratio curve is generated for a range of incident angles: the response ratio at $\theta = 0^\circ$ is the optical concentration ratio.

4.2.1 The Effect of a Polygonal Cross-section

In this section, we wish to investigate the effect of the polygonal, rather than circular, cross-section. For the purpose of the simulations, we assume an ideal reflector, which has a reflectance of 100%. We also assume that the reflectance of the photocathode is 0%, and that its efficiency is 100 %.

If a concentrator has a polygonal cross-section, and it is meant to be used with a spherical absorber, then two effects will degrade the performance of the concentrator. First, the profile across opposite vertices is different from the profile across the narrow width of the polygon (see fig 4.20). It is stretched radially by a factor of $1/\cos(\pi/N)$, where N is the number of sides. It no longer has the optimal shape. Secondly, there will be gaps between the concentrator and the spherical absorber. This will produce a dip in the performance curve at $\theta = 0^\circ$, since most rays at that angle are destined to reach the absorber out of bounds, without the benefit of the concentrator.

The performance curve for different polygonal cross-sections is shown in figure 4.22.

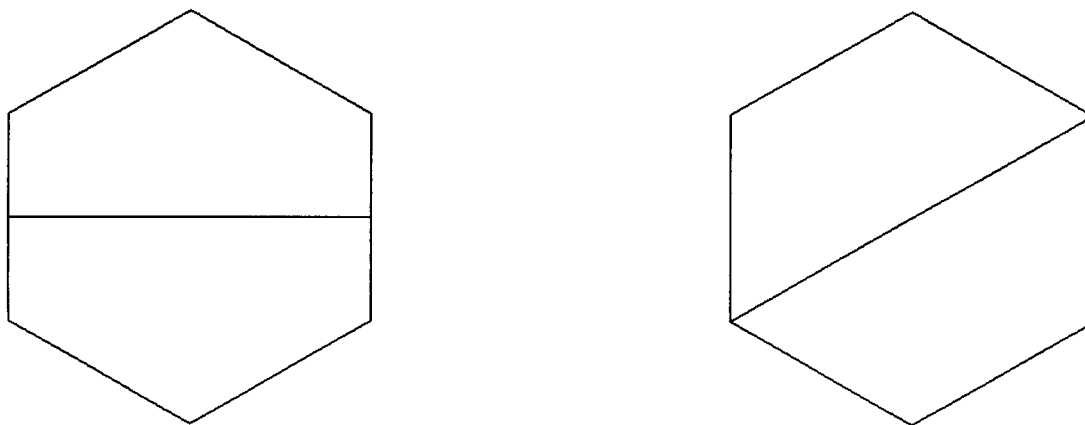


Figure 4.20: The profile is different in two orientations.

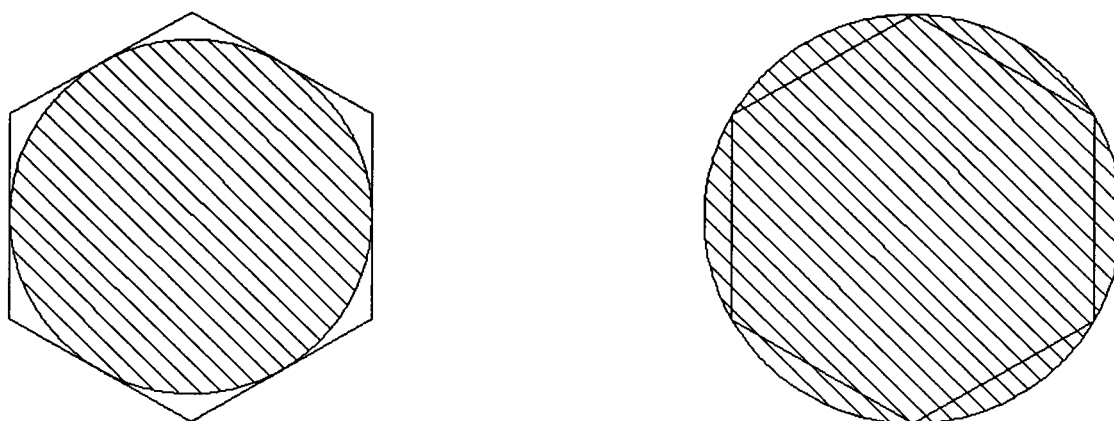


Figure 4.21: Demonstrating the relationship of the concentrator's polygonal exit aperture to the acceptance area of the absorber (shaded). On the left is a normal aperture, on the right is a modified aperture.

Number of sides	Percentage sensed	Percentage lost	Expected
6	75	25	17
12	90	10	4.5
20	96.5	3.5	2
30	98	2	1

Table 4.1: Performance at $\theta = 0^\circ$ incidence.

There is an obvious dip at 0° . Table 4.1 lists the percentage of the rays which reach the photocathode when the source is incident at 0° , for a number of different polygonal cross-sections. These simulations show that only 75 % of the rays reach the photocathode when the cross-section is hexagonal, for example. One would naïvely expect that the fraction of rays lost in the gaps would be of the order of the area of the gaps, relative to the entry aperture area. The last column in Table 4.1 shows the area of the gaps as a percentage of the area of the entry aperture. The percentage of rays lost is higher than this, showing that the rays are concentrated near the rim of the exit aperture.

There is also a smaller effect on the drop-off in the performance curve near the cut-off angle (see figure 4.23). It is most marked for the hexagonal case, but the performance is much better when the number of sides is increased. The performance in Figures 4.22, 4.23, and in Table 4.2 follows the normalization convention for a source infinitely far away: it must be multiplied by $\cos \theta$ for comparison with measured values. We can define the spread as the range of angles over which the performance drops from 90 % to 10 %.

There is a way to regain the rays lost through the gaps. It consists in enlarging the acceptance angle of the absorber, or in designing the concentrator with a smaller exit aperture (see fig 4.21). This remedies the dip in the performance curve near $\theta = 0^\circ$,

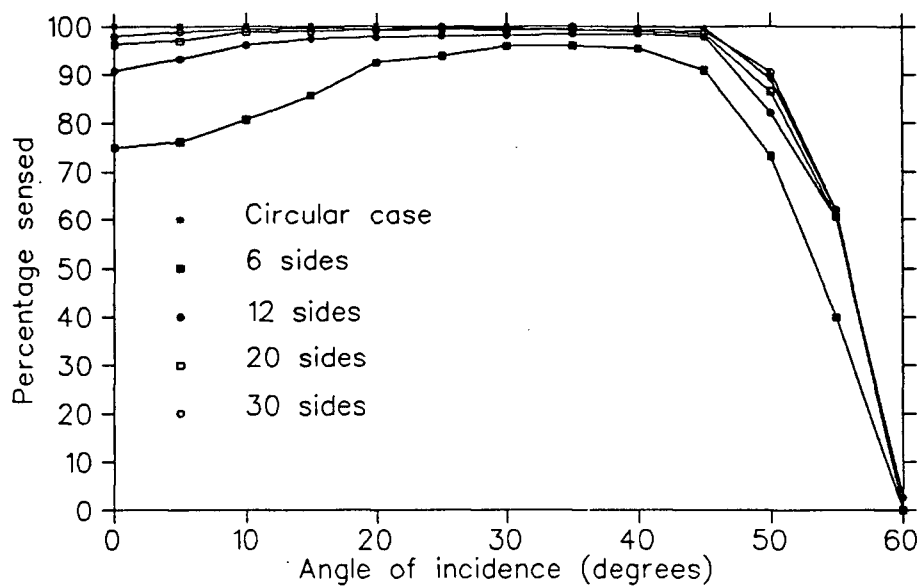


Figure 4.22: The performance curve for different cross-sections.

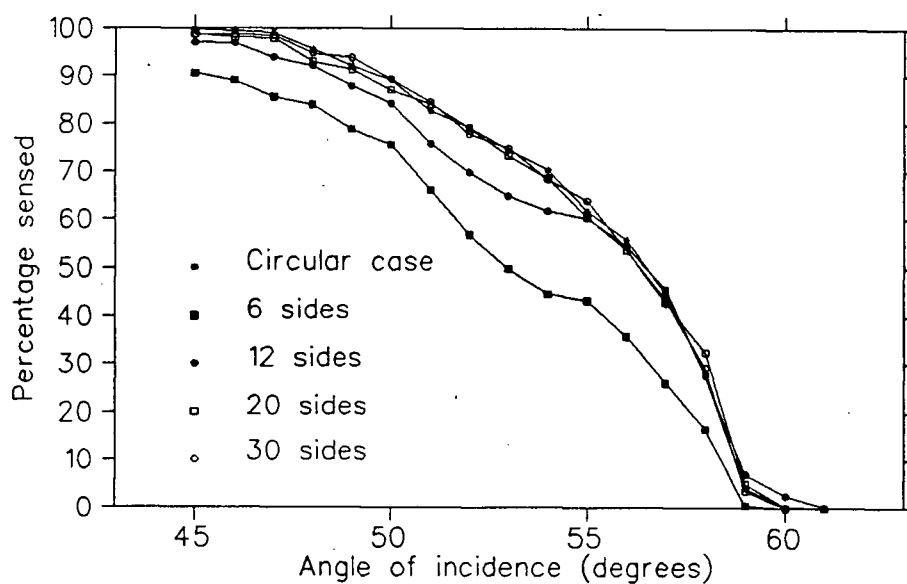


Figure 4.23: Detail of the previous curve.

Number of sides	Spread
6	14°
12	10°
20	9°
30	9°
circle	9°

Table 4.2: Performance near the cut-off angle.

at the expense of reducing the concentration factor. But this can be worth it, because it captures rays which would otherwise be lost. For example, the concentration ratio for the dodecagonal concentrator is reduced by 10% , from 1.875 to 1.69, on account of rays lost through the gaps. If the acceptance radius of the absorber is increased by a factor of $1/\cos 15^\circ$, then the concentration ratio goes from 1.875 to 1.79, a drop of only 4.5% , since all the rays are kept.

4.2.2 The Reflection Properties of Flat TIRF

The range of incident angles which result in total reflection from one layer of TIRF is severely limited. Consider polycarbonate TIRF, with $n \simeq 1.6$. For rays whose projection onto the surface is parallel to the x-axis, only rays within 10.6° of normal will undergo total internal reflection from TIRF in air. This angle is greater for rays whose projection is closer to the TIRF ridges, the y-axis (see Chapter 3). If one is to use TIRF to form a concentrator, the angular range needs to be considerably expanded. This can be achieved by using several layers; light rays transmitted by one layer emerge rectified, and have a second chance of reflection.

In water, the relative index of refraction is smaller, $n \simeq 1.6/1.33 \simeq 1.2$. Rays with projections parallel to the x-axis will not undergo total internal reflection, and we have to rely on partial reflections at interfaces with the plastic. Adding more layers increases

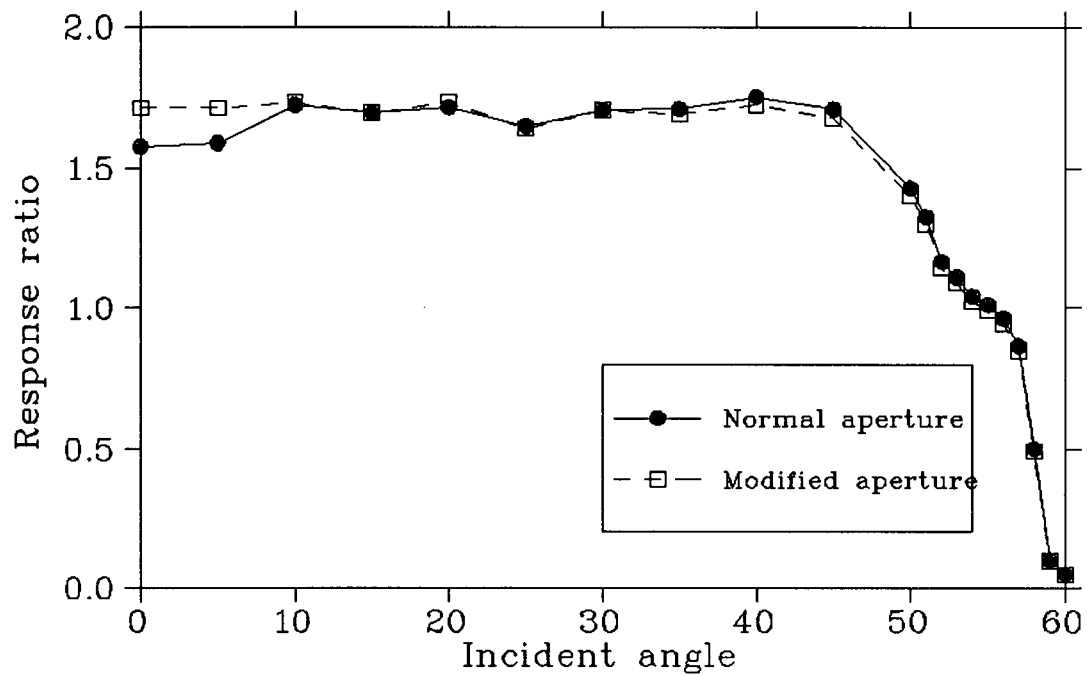


Figure 4.24: Two response ratio curves for a dodecagonal concentrator. In the first case, the acceptance area of the PMT fits within the dodecagonal exit aperture of the concentrator. In the second case, the acceptance area is enlarged.

$\lambda(\text{nm})$	Absorption Length (mm)	Refractive Index
300	4.2	1.675
325	7.6	1.655
350	50	1.635
400	> 100	1.613
500	> 100	1.584
600	> 100	1.580

Table 4.3: Optical properties of Polycarbonate Plastic.

the possibility of partial reflections occurring.

A ray-tracing code has been generated to study the properties of multiple layers of TIRF. This code employs Monte-Carlo techniques, ignoring polarization effects, which are expected to be negligible in this situation. The incident rays have a spectrum typical of that observed in Čerenkov detectors (300-600nm, with a peak at 375nm) and the TIRF refractive index and absorption length are modelled appropriately as functions of wavelength (see Table 4.3).

Figures 4.25 and 4.26 show the probabilities of reflection (in any direction) for incident rays whose projection on the TIRF surface is parallel to the x-axis. The reflectances were evaluated at 1° intervals using 1000 rays per angle.

Figure 4.25 shows the case for TIRF in air. Only rays close to normal undergo “antispecular” total internal reflection in one pass. The angular region in which this occurs is well defined (in fact this was the means by which the refractive index was determined as a function of wavelength). Outside this region more reflections are required and some rays are lost. More layers increase the total reflectivity. As the angle comes close to 90° , partial reflections from the first surface dominate.

The enhancement at $20 - 40^\circ$ in the two-layer case arises because light transmitted by the first layer is deviated sufficiently to allow total internal reflection at the second

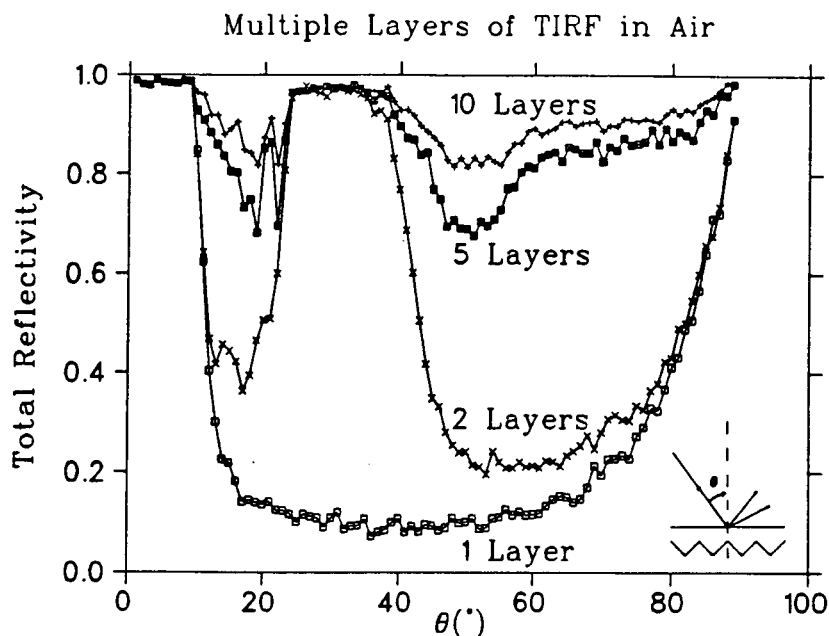


Figure 4.25: Reflection from multiple layers of TIRF in air.

layer.

Figure 4.26 shows the case for TIRF in water. Here only partial reflections are important and the improvement with more than two layers is significant.

4.2.3 The Effect of the Reflection Properties of TIRF

In this section, we will compare the performance of an ideal concentrator to that of a fictitious circular TIRF concentrator. The ideal concentrator has a circular cross-section and fits snugly on the photocathode, and it is perfectly reflective. The circular TIRF concentrator has the same shape, but has the reflection properties of TIRF. It is impossible to achieve in practice, because TIRF does not bend well into a concentrator with a circular cross-section (see chapter 3).

Figure 4.27 compares the response ratio curve for TIRF in air, for the cases of 1, 3, 5, and 10 layers, as well as for an ideal specular reflector. The performance is quite

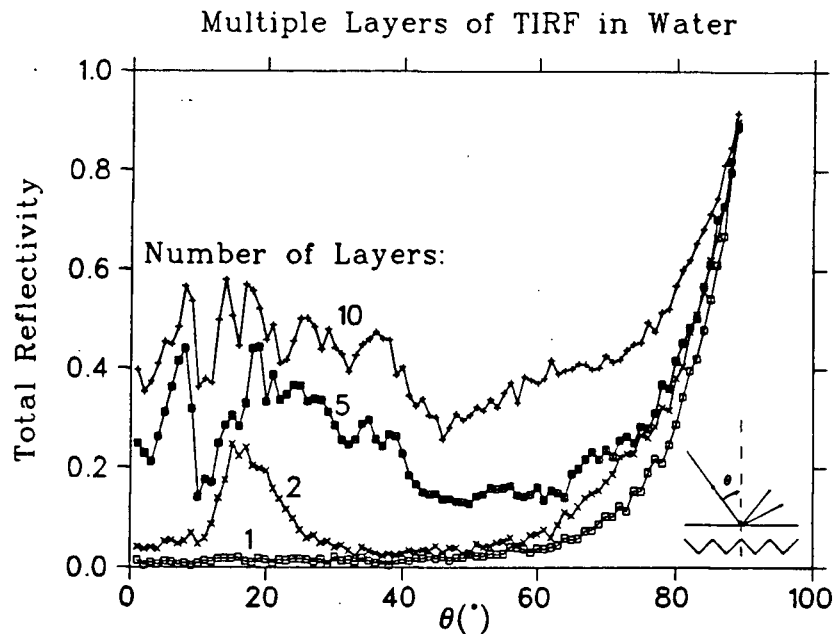


Figure 4.26: Reflection from multiple layers of TIRF in water.

good, even for 5-layer TIRF. The advantage in TIRF's total internal reflection for near y-axis rays is clear. However, TIRF does not perform so well at larger angles and the cut-off is not so sharp as for a specular surface.

Figure 4.28 compares the response ratio curve for TIRF in water, for the cases of 1, 3, 5, and 10 layers, as well as for an ideal specular reflector. The performance is poor, even for 10-layer TIRF. The response ratio is good near $\theta = 0$, but it drops too much too soon. There doesn't seem to be a great difference between the 5- and 10-layer cases.

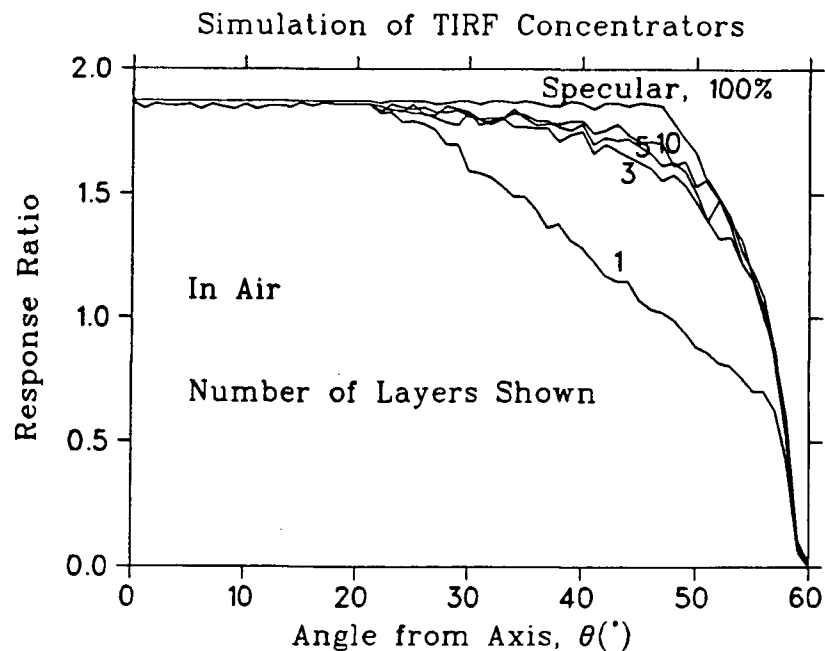


Figure 4.27: Performance of an idealized circular-section TIRF concentrator in air.

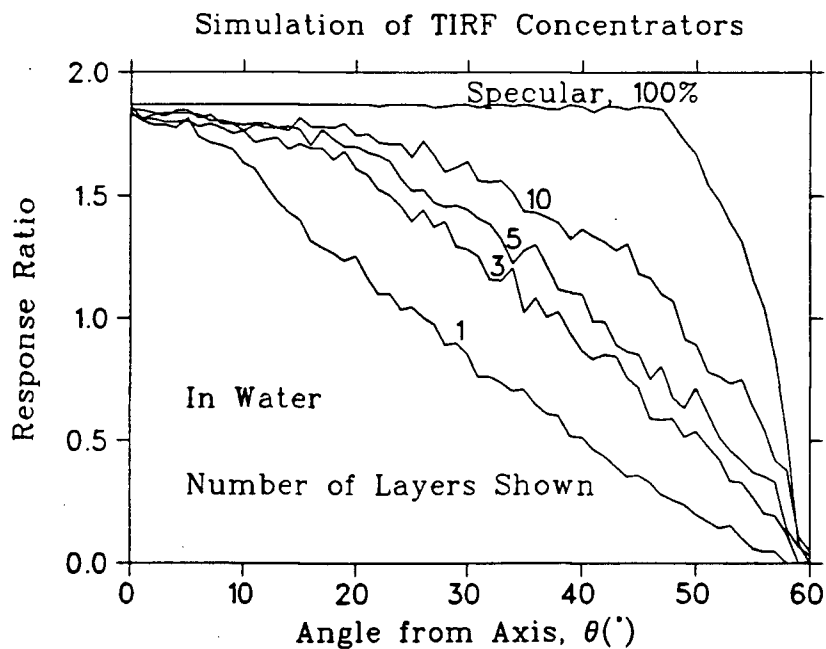


Figure 4.28: Performance of an idealized circular-section TIRF concentrator in water.

Chapter 5

Prototype Tests and Results

In this chapter, we present the testing of two prototype TIRF concentrators which have been built at UBC. Their profiles were generated according to the two-dimensional theory of Chapter 2; the radial coordinate R was taken to define the short radius of the polygonal cross-section of the concentrator. The polygonal exit aperture was designed to fit around the sensitive area of the photocathode.

We also present the results of tests performed on a spun-aluminum concentrator which was made by Harjohn Ltd. of St. Catharines, Ontario. This concentrator has a circular cross-section.

The photocathode is approximately spherical, and the sensitive area is defined as a section of this sphere; it is described by the polar angle (θ_c in Chapter 2) and the cylindrical polar radius ($R \sin \theta_c$, where R is the spherical radius).

5.1 Data Taken at Oxford

The first prototype TIRF concentrator was designed for an EMI tube, which had a polar radius of 10.2 cm and a polar angle of 68° . The acceptance angle chosen was 47° ; this gives an entrance aperture radius of 17.9 cm, a length of 27.6 cm, and a geometrical concentration ratio of 2.85. The concentrator was truncated to 18 cm, reducing the concentration ratio to 2.7. The cross-section was hexagonal, and the petals were made of 10 layers of TIRF.

The prototype was taken to Oxford by C. E. Waltham and tested there on a facility

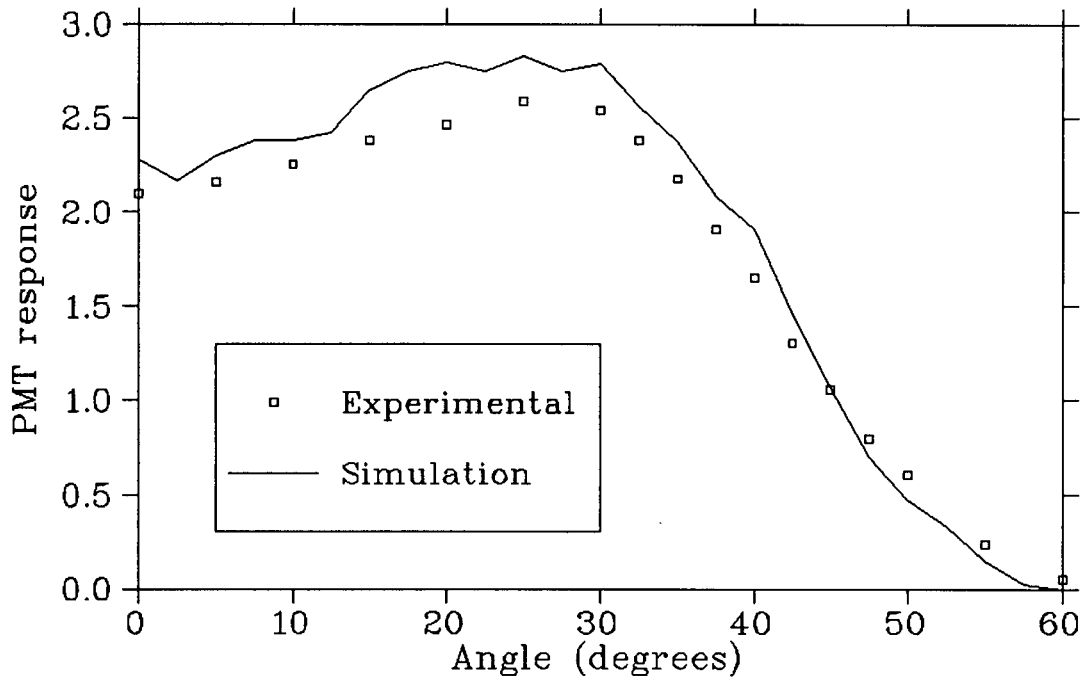


Figure 5.29: The performance of the first UBC prototype.

with a parallel light beam. The intensity of the detected light was measured using the anode current of the PMT. The response ratio curve was normalized to the intensity measured at $\theta = 0^\circ$ with the concentrator removed. The response ratio curve was corrected by dividing it by a factor of $\cos \theta$: this normalization corresponds to a uniform distribution on the entrance aperture which is independent of the incident angle.

Figure 5.29 shows the response ratio curve for this first prototype. The concentration ratio at normal incidence is low (2.10), and the drop-off is very wide (20° , compared to 10°). Originally, the performance of the TIRF concentrator was compared to the performance of an ideal, circular-section specular concentrator. The bad performance was originally attributed to the reflection properties of TIRF and the hexagonal cross-section, which leaves huge gaps between the concentrator and the PMT. While it is true that these degrade the performance of the concentrator, they are not enough to explain it completely. The computer code was modified to account for the polygonal

cross-section of the concentrator. It was then found that the major culprit was a mismatch between the concentrator and the tube. The actual EMI tube had a polar angle of 60° (rather than 68°) and a polar radius of 9.5 cm (rather than 10.2 cm). This meant that the rays were not aimed optimally. Also, since the concentrator was too large, it was placed incorrectly on the PMT: it was displaced 3 mm “downwards” in the z direction.

Another concern is an inaccuracy in Moorhead’s original code. This computer code assumes systematically that if a reflected ray aims directly at the entrance aperture, then it is lost. It must be remembered that the PMT is curved (approximately spherical), and sometimes the ray is detected by the PMT instead. This inaccuracy makes the simulated performance drop earlier and faster than the actual performance. Once all these modifications were incorporated in the code, the data could be simulated more accurately. It was then decided to design a dodecagonal, rather than hexagonal, concentrator.

5.2 TIRF tests at UBC

A second prototype was built at UBC. It was designed to fit the Hamamatsu PMT, and to have a dodecagonal rather than hexagonal cross-section. The Hamamatsu PMT is not perfectly spherical; the profile of the tube is approximately described by a sphere with a cylindrical polar radius of 9.5 cm, and a polar extent of 54.5° . The cut-off angle of the concentrator is 58.6° , which yields an entrance aperture radius of 13.0 cm, and a geometrical concentration ratio of 1.875. Since the height is only 14.9 cm, truncation was not deemed necessary.

The cylindrical polar radius of the sensitive area of the Hamamatsu photomultiplier tube is about 10 cm, but the concentrator was designed to have a dodecagonal exit

aperture with a short radius of 9.5 cm (and a long radius of 9.84 cm). The intent was to limit the amount of light which would fall through the gaps and beyond the sensitive area. The actual prototype has a short radius of 9.7 cm (long radius 10 cm). For definiteness, the sensitive area of the Hamamatsu tube was defined, using black tape, as a circular opening fitting the acrylic frame (9.85 cm radius).

5.2.1 Experimental Apparatus

Two light-tight optical cavities were used to test the concentrator: a large one, and a smaller, water-tight one. In order to simulate Čerenkov light, we used ^{241}Am , an α -emitter. It was mounted on a small NE102 scintillator, which was coupled by an acrylic light-pipe to a 2" RCA 8575 PMT. In the large cavity, the small PMT was mounted horizontally on a rotating arm 99 cm in length. This arm was centered on a point 3.1 cm inside the Hamamatsu tube. The small, water-tight cavity had a black lid; the small PMT was mounted on it vertically. The light source was inserted through holes at 15-degree intervals, around a circle 75.2 cm in radius, centered on a point 2.3 cm inside the Hamamatsu PMT. A pair of Helmholtz coils 87 cm in radius compensated for the Earth's magnetic field; they were adjusted for the local magnetic field. This tank is depicted in figure 5.30.

The TIRF concentrator had a tendency to trap air bubbles between the layers of TIRF. Trapping air between the sheets of TIRF would increase the reflectance, but the bubbles are random and the reflected light would be scattered. Eventually, if the concentrator were left in the SNO detector for an extended period of time, the bubbles would dissolve in the de-gassed water, and the concentrator would lose these bubbles. In order to have a realistic assessment of the properties of the TIRF concentrator, great

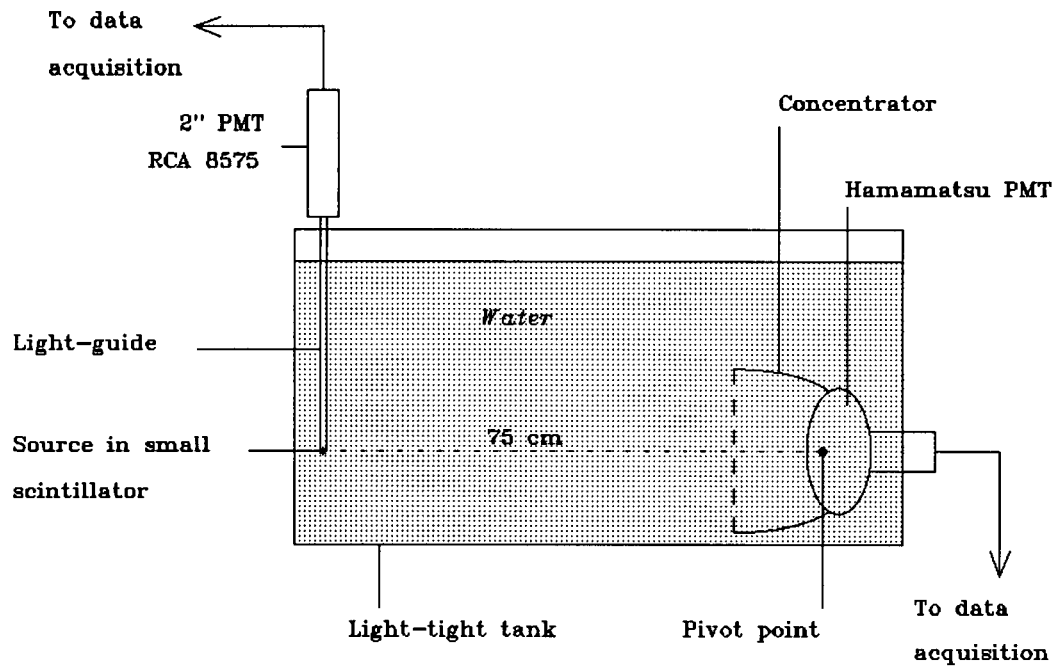


Figure 5.30: Experimental apparatus. The light source is placed at points along a circle centered on the pivot point, towards and away from the reader. A pair of Helmholtz coils (not shown) surrounds the Hamamatsu tube.

care was taken to minimize the amount of air trapped by the concentrator. Nevertheless, a few bubbles remained trapped near the rim of the entrance aperture.

5.2.2 Data Acquisition

In order to determine the intensity of the light, we analyzed the pulse height spectrum of the Hamamatsu tube. We required coincidence with the RCA PMT in order to reduce background noise.

The data acquisition system is depicted diagrammatically in figure 5.31. Basically, the signal from the Hamamatsu tube is amplified and sent to the pulse height analyzer (PHA); it is gated by coincidence with the RCA PMT. When the signals from the Hamamatsu and RCA tubes are in coincidence, the coincidence unit generates a gate signal for the PHA. A Constant Fraction Discriminator (CFD) provides rejection of noise for each signal. The scaler-gate unit lets the experimenter generate a veto signal to initiate and terminate a run. The attenuator circuit is used for calibration purposes.

The intensity of the light was assessed according to the first moment of the coincidence pulse height spectrum. If N is the channel number, and $f(N)$ is the number of counts in channel x , then the first moment is: $I = \sum_{N=0}^{511} N \cdot f(N)$. Measurement runs lasted 500 sec, and the ^{241}Am source had a count rate of 10 kHz. Typically, the coincidence count rate varied from roughly 182 000 at $\theta = 0^\circ$, down to 16 000 at $\theta = 60^\circ$, and the first moment varied from 11 000 000 down to 370 000. The offset was 19.53, and the first 20 channels were rejected. This permitted a reproducibility at the level of 2%. The normalization factor was determined by measuring the intensity at $\theta = 0^\circ$ with the concentrator removed.

The detection efficiency of the Hamamatsu photocathode was not uniform. It was measured using a coincidence arrangement as above, but the source was placed right on

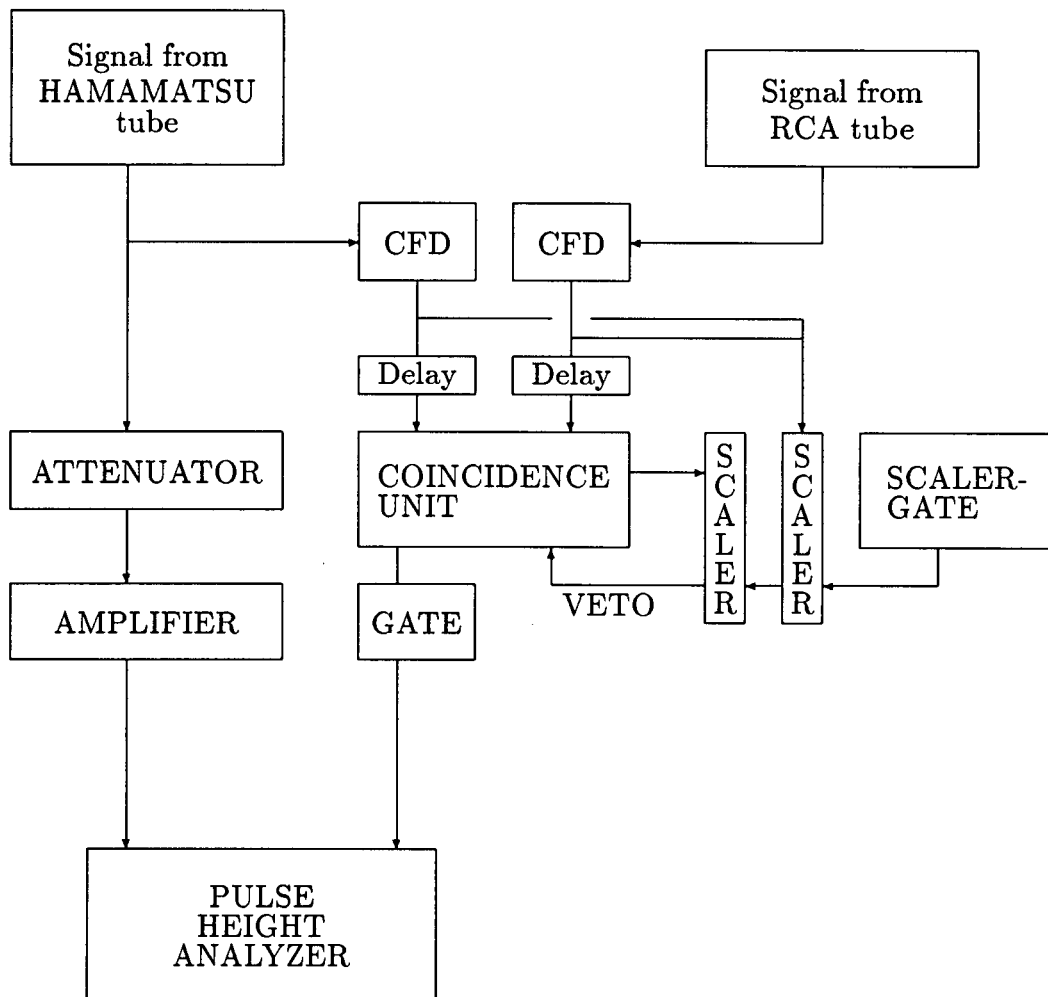


Figure 5.31: The data acquisition system.

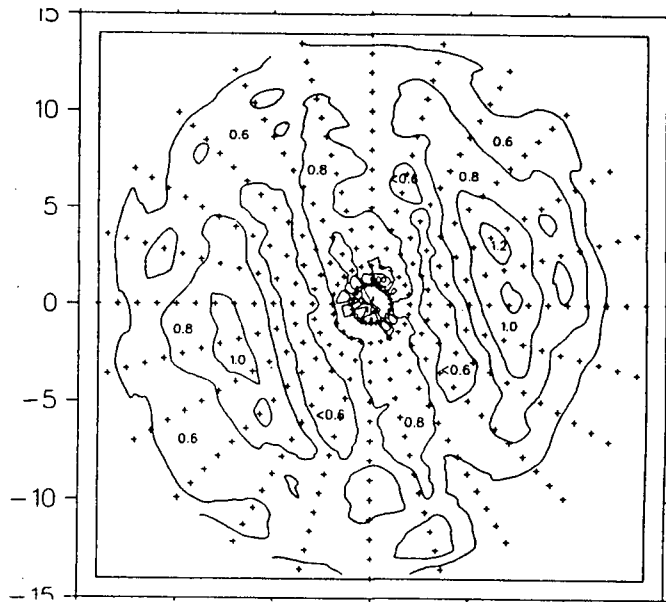


Figure 5.32: Map of the efficiency variations on the photocathode.

the surface of the tube. The map of the sensitivity is shown in figure 5.32. The crosses indicate sampling points; the contours were generated by interpolation. By convention, the center has a sensitivity of 100%. There are two bands on either side, where the sensitivity drops to 50%, and then two more bands, where the sensitivity rises to 120%. These corrections were included in the simulations.

5.3 Results

Figure 5.33 shows the response ratio curve for the case of the TIRF concentrator in air, in the large tank. The concentration ratio rises up to 2.71, but this is because the source is a finite distance away. The computer code simulates this as well as the optical properties of TIRF, and the non-uniformity of the Hamamatsu efficiency. The agreement between the data and the simulation is very good.

Figure 5.34 shows the response ratio curve for the TIRF concentrator in air again,

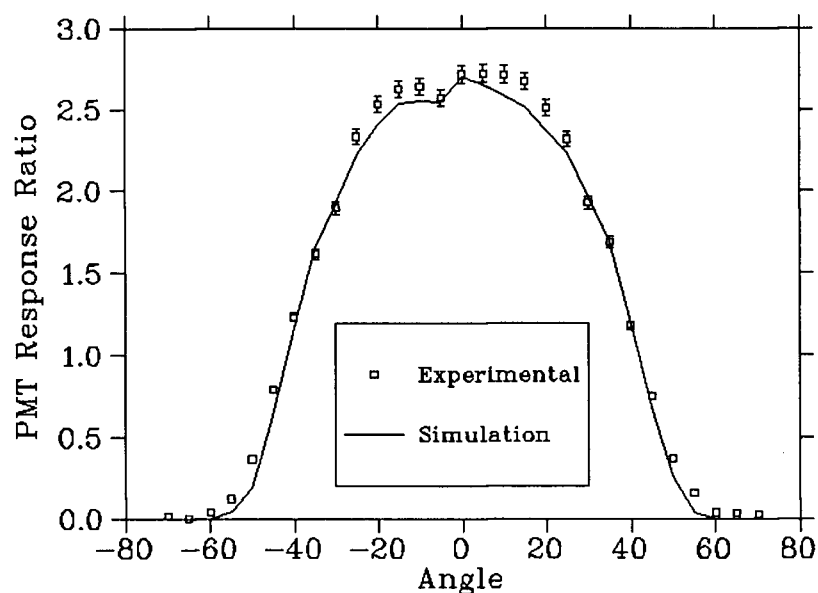


Figure 5.33: TIRF in air on the long rotating arm (99 cm).

but this time, in the small tank. The agreement between the simulation is fairly good, but not as good as in the previous case. The concentration ratio at normal incidence drops from 2.72 to 2.65, while the theoretical value increases from 2.70 to 2.74. There might be effects due to the non-uniformity of the tube: at normal incidence, the light is concentrated near the rim of the sensitive area, where the efficiency changes the most rapidly.

Figure 5.35 shows the response ratio curve for the TIRF concentrator in water (in the small tank). Again, the agreement between data and simulation is fairly good. The experimental data shows a tail at high angles, which could be caused by light scattered from the walls of the tank, and by small air bubbles trapped between the layers of TIRF.

Even though great care was taken to minimize the amount of air trapped by the

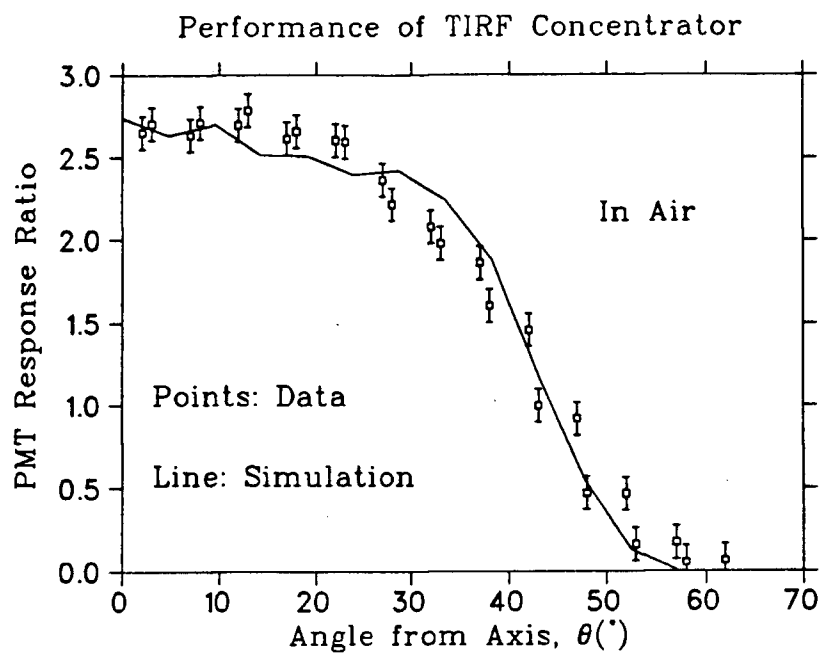


Figure 5.34: TIRF in air in the smaller tank (75 cm).

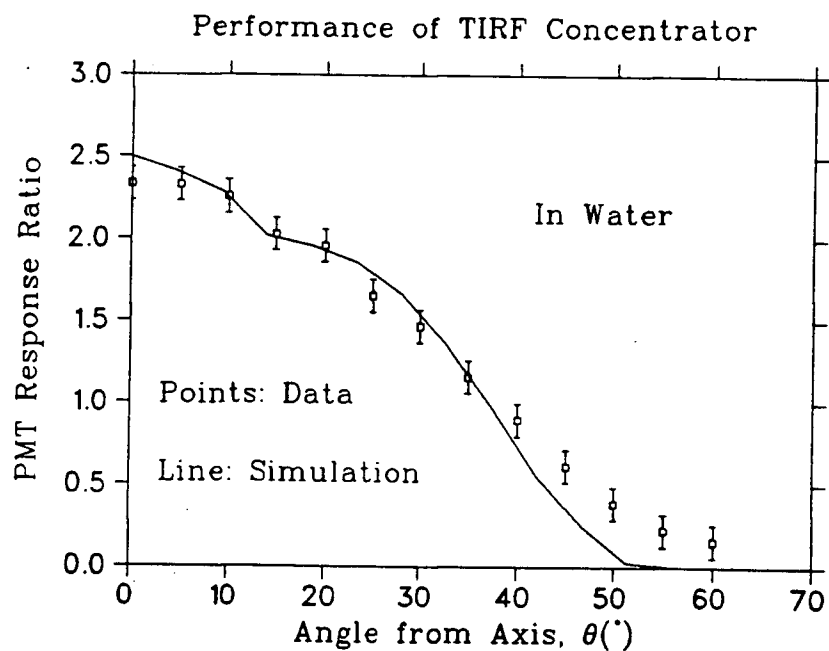


Figure 5.35: TIRF in water in the smaller tank (75 cm).

They would not affect the performance near $\theta = 0^\circ$, because they subtend a small solid angle, and the TIRF is reflective in this perspective anyway. However, they could enhance the reflectance near the cut-off angle, because they subtend a larger solid angle, and the TIRF is not normally very reflective at that perspective.

5.4 Aluminum tests at UBC

Tests have also been performed on an aluminum cone produced at Carleton University. This cone does not have the optimal profile, and it is smaller, but the cross-section is circular. The entrance aperture radius is 11.1 cm, the exit aperture radius is 7.9 cm, yielding a geometrical concentration ratio of 1.97 .

The response ratio curve of this aluminum cone is shown in figure 5.36. There is a small difference between the data taken in air and in water: the reflectance of aluminum in air is 85%, and in water, 83%.

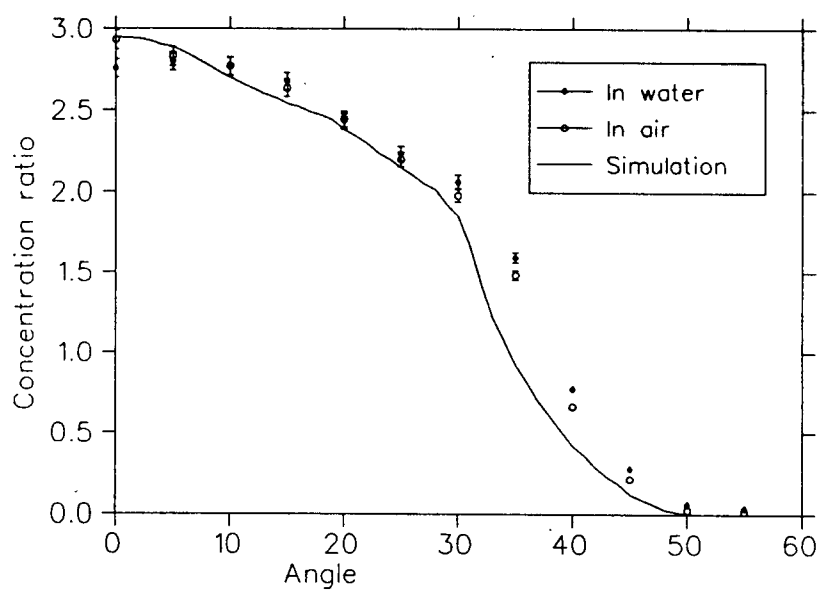


Figure 5.36: Aluminum cone in the smaller tank (75 cm). The continuous line shows the simulation for a concentrator in air, with a reflection of 85%.

Chapter 6

Discussion

The performance of the TIRF concentrator in air is comparable to that of concentrators made from the best specular materials. However, the angular response in water is much worse than in air. The performance of the TIRF concentrator in water could be improved by sealing air between the sheets of TIRF. This enhances the relative refractive index, and total internal reflection occurs for a wider range of angles.

Sealing air between the sheets of TIRF presents some challenges, since water tends to diffuse through the TIRF material. The diffusion rate is such that on the time-scale of the SNO experiment, the gaps would soon be full of water. For the purposes of the SNO experiment, the seal must be transparent to ultra-violet light, and it must survive many years in water. Sealing might be accomplished by wrapping the concentrator in a transparent film, but the support system for the TIRF concentrator complicates this task. Each layer has twelve petals, which are held together by keeping the sheet in one piece, and the petals are bent outward where they meet the acrylic frame. An alternative would be to place the TIRF sheets in a transparent plastic bowl, which would provide support while sealing the concentrator.

An aluminum concentrator of satisfactory design has been chosen for the SNO detector, however we believe that TIRF concentrators have particular merits and may find application elsewhere. They are inexpensive, and contain no metal and very little radioactive impurities. They must have a polygonal cross-section, which can degrade the performance, but this drawback can be overcome. For short periods of immersion

in water, the TIRF stack may be sealed well enough to contain air between the layers.

Bibliography

- [1] *SNO Collaboration*:
Queen's University, National Research Council of Canada, Chalk River Nuclear Labs., University of Guelph, Laurentian University, Carleton University, University of B.C., U.C. Irvine, Princeton University, University of Pennsylvania, Los Alamos National Lab., Lawrence Berkeley Lab., Oxford University.
- [2] W.T.Welford and R. Winston, *The Optics of Nonimaging Concentrators: Light and Solar Energy*, Academic Press, New York, 1978
- [3] J.N.Bahcall, *Neutrino Astrophysics*, Cambridge University Press, 1989
- [4] R.Davis Jr., in *Neutrino '88*, Proceedings of the 13th International Conference on Neutrino Physics, ed. J.Schneps et al. (World Scientific, Singapore, 1989).
- [5] TIRF is available from TIR Systems Ltd, 3935 2nd Ave, Burnaby, B. C., Canada V5C 3W9
- [6] Lorne A. Whitehead, *Transport and Distribution of Light Energy for Illuminating Engineering Applications*, Ph.D. thesis, University of British Columbia, Dept. of Physics, 1989.
- [7] Max Born and Emil Wolf, *Principles of Optics*, Sixth (corrected) edition, Pergamon Press, Oxford, 1987.
- [8] J.N.Bahcall and R.K.Ulrich, *Rev. Mod. Phys.* **60** (1988) 297.
- [9] K.S.Hirata, T.Kajita, T.Kifune, K.Kihara, M.Nakahata, K.Nakamura, S.Ohara, Y.Oyama, N.Sato, M.Takita, Y.Totsuka, Y.Yaginuma, M.Mori, A.Suzuki, K.Takahashi, T.Tanimori, M.Yamada, M.Koshihara, T.Suda, K.Miyano, H.Miyata, H.Takei, K.Kaneyuki, Y.Nagashima, Y.Suzuki, E.W.Beier, L.R.Feldscher, E.D.Frank, W.Frati, S.B.Kim, A.K.Mann, F.M.Newcomer, R.Van Berg, and W.Zhang, *Phys. Rev. Lett.* **63** (1989) 16.
- [10] S.P.Mikheyev and A.Yu.Smirnov, *Nuovo Cimento* **C9** (1986) 17.
- [11] L.Wolfenstein, *Phys. Rev.* **D17** (1978) 2369 and **D20** (1979) 2634.

- [12] M. E. Moorhead and N. W. Tanner, The Concentration of Light onto Near-Spherical Photomultipliers, Nucl. Inst. Meth., to be published.
- [13] M. E. Moorhead and N. W. Tanner, Optical Properties of the K-Cs Alkali Photocathode, Oxford University preprint OUNP-91-05, Nucl. Inst. Meth., to be published.
- [14] Guy R. Ouellette, C. E. Waltham, R. Meijer-Drees, A. Poon, R. Schubank, and L. Whitehead, Nonimaging Light Concentration Using Total Internal Reflection Films, Applied Optics, to be published.